UNIVERSIDADE DE LISBOA
FACULDADE DE CIÊNCIAS
DEPARTAMENTO DE ENGENHARIA GEOGRÁFICA, GEOFÍSICA E ENERGIA

Changes in the surface energy balance over areas affected by wildfires: a diagnostic study in Continental Portugal

Maria Inês Buco Cajada

Mestrado em Ciências Geofísicas
Especialização em Meteorologia e Oceanografia

Dissertação orientada por:
Doutora Sofia Ermida
Professor Doutor Carlos da Camara

2021

Acknowledgements

I woud like to give special thanks to my supervisors Doctor Sofia Ermida and Professor Carlos da Camara for their support, availability and advice. Thank you for always motivating me to do better.

I would also like to thank my family and friends for always believing in me and encouraging me to follow my dreams.

This work was done in the framework of a research scholarship funded by EUMETSAT LSA-SAF (Satellite Application Facility on Land Surface Analysis).

Abstract

The Mediterranean region is recurrently affected by large wildfire events. Because of climate change associated to anthropogenic factors, wildfire events have become more frequent and have been affecting larger areas, and it is likely that the problem will become even more serious in the near future. It is therefore important to better understand the impacts of large wildfire events both on surface parameters and surface energy balance.

Downward surface shortwave and longwave fluxes (DSSF, DSLF), surface albedo (AL), surface emissivity (EM) and land surface temperature (LST) are retrieved from the Satellite Application Facility on Land Surface Analysis (LSA-SAF). Besides analysing each parameter, this work uses this information to study longwave and shortwave radiation (LW, SW) balances and the surface net radiation.

Based on the analysis of 5 different areas affected by wildfires in 2020, it can be inferred that, as seen in previous studies, DSSF and DSLF do not show significant changes after the fire, AL and EM show a decrease, especially for the larger burned areas, and LST presents an increase between 1.5℃ and 10℃ after the fires. This increase in LST is the main cause for the increased differences, between averaged values for burned (BB) and unburned (UB) pixels, in the LW balances that lead to changes in net radiation.

The LSA-SAF also disseminates data computed using a surface balance model (SEB), namely evapotranspiration (EVAP), sensible and latent heat fluxes (H, LE), and skin temperature (TSK). A comparison between TSK and LST shows that the model is not well representing the surface behaviour. Moreover, a comparison of the net radiation results obtained with the SEB model with the ones obtained through remotely sensed data indicates that LE and H are not enough to characterize the net radiation and therefore the ground heat flux (G) cannot be neglected.

Keywords

Wildfires, Remote Sensing, Surface Energy Balance, Land Surface Temperature, Surface Heat Fluxes

Resumo

A região mediterrânica é recorrentemente afetada por grandes incêndios florestais. As alterações climáticas associadas a fatores antropogénicos, têm vindo a tornar episódios de fogo mais frequentes e a afetar maiores áreas. Torna-se, assim, cada vez mais premente entender os impactos dos grandes incêndios florestais, especialmente sobre os parâmetros de superfície e sobro o balanço de energia.

O presente trabalho utiliza dados, obtidos através de deteção remota por satélite, disseminados pela *Satellite Application Facility on Land Surface Analysis* (LSA-SAF). Os dados baseiam-se em observações efetuadas pelo *Spinning Enhanced Visible and Infrared Imager* (SEVIRI), o radiómetro a bordo dos satélites da série *Meteosat Second Generation* (MSG). Os dados de satélite disseminados e analisados neste trabalho consistem nos fluxos radiativos à superfície de ondas curtas e longas (*downward surface shortwave and longwave fluxes* – DSSF, DSLF), no albedo (AL), na emissividade (EM) e na temperatura de superfície do solo (*land surface temperature* – LST). Estes dados permitem estudar as alterações nos balanços radiativos de ondas curtas (*shortwave radiation* – SW) e longas (*longwave radiation* – LW) e no balanço radiativo (resultante da combinação dos dois primeiros balanços) e avaliar o impacto dos incêndios nas propriedades da superfície e no balanço energético. Neste trabalho foram analisadas cinco áreas afetadas por incêndios em 2020, quatro das quais em Portugal e uma em Espanha.

Para além dos dados de satélite, a LSA-SAF também dissemina dados obtidos através de um modelo de balanço de energia à superfície (*surface energy balance* - SEB), nomeadamente a evapotranspiração (EVAP), os fluxos de calor sensível e latente (*sensible and latent heat fluxes* – H, LE) e a temperatura da pele (*skin temperature* – TSK). Com o objetivo de analisar o desempenho do modelo, efetuaram-se comparações entre os resultados obtidos pelo modelo SEB e os resultados derivados de observações de satélite.

Para cada uma das áreas estudadas, selecionaram-se conjuntos de pixéis queimados (*burned* – BB) e não queimados (*unburned* – UB) e procedeu-se a uma comparação sistemática do comportamento dos parâmetros selecionados antes e após os eventos de incêndio. Os dados considerados foram entre as 12h e as 14h30 UTC, período de tempo que, em geral, inclui o máximo diário de LST. A fração do ano considerada, entre maio e outubro de 2020, que contém um número suficiente de observações por satélite, é adequada para analisar o comportamento das variáveis escolhidas.

A análise dos resultados obtidos através de dados de satélite está em concordância com resultados de estudos anteriores. A DSSF e a DSLF não mostram diferenças significativas após os incêndios, um resultado esperado considerando que estes fluxos não dependem das características do solo. O AL e a EM sofrem uma descida nos pixéis BB após o incêndio, sendo a descida mais acentuada nos incêndios onde a área queimada é maior. Com o escurecimento do solo e diminuição da densidade de vegetação, é de esperar que a LST aumente após a ocorrência de um incêndio, o que, de facto, se observou. A LST aumenta em todos os casos estudados entre 1.5℃ e 10℃. No caso do balanço de SW, observam-se anomalias que são consistentes com as anomalias observadas no AL. Já no caso do balanço de LW, tem-se, na maior parte dos casos, um aumento absoluto da radiação LW que sai dos pixéis BB, a qual resulta do aumento de LST. O impacto das anomalias de EM neste balanço é mais difícil de analisar considerando que as estimativas são utilizadas para estimar a LST. Em 4 dos 5 casos, observa-se uma anomalia no balanço de LW que é superior à no balanço de SW. Assim sendo, quando se calcula o balanço total de radiação, como sendo a soma dos balanços de SW e LW, observam-se anomalias no sentido das anomalias do balanço de LW. Tem-se, assim, para a maioria dos eventos, uma diminuição do balanço total de radiação depois de um incêndio, a qual resulta do maior aumento de LW libertada para o espaço em comparação com a absorção de SW.

Na análise do modelo SEB, começa por comparar-se a TSK com a LST, pois, para uma boa representação das alterações das características do solo, a TSK deve seguir de perto o comportamento da LST. Apesar de, mostrar um aumento tal como a LST, o aumento da TSK é significativamente menor, no máximo metade do observado na LST. A EVAP, bem como o LE que resulta da EVAP, mostram uma diminuição após os incêndios. Este resultado é expectável considerando a diminuição/extinção de vegetação provocada pelo incêndio. No caso de H, tendo em conta o aumento da temperatura à superfície, é esperado um aumento de H após o incêndio. Este aumento é observado na maior parte dos casos. Utilizando os dois fluxos de calor sensível e latente à superfície (H e LE) e desprezando o fluxo de calor do solo (*ground heat flux* – G), pode-se estimar o balanço total de radiação da superfície como sendo a soma de H e LE mas, neste caso, ao contrário dos resultados obtidos quando se somam os balanços de SW e LW (baseados nas observações por satélite) não se observa nenhuma alteração após o incêndio. Este resultado sugere que se averigue qual o impacto do fator G no cálculo do balanço. Recalculou-se, portanto, o balanço total de radiação total à superfície como sendo a soma dos fluxos H, LE e G, sendo de notar que, uma vez que, neste trabalho, G é obtido através de dados de satélite, pode não corresponder ao valor estimado que é calculado pelo modelo (o qual resulta da resolução da equação de balanço de energia). Apesar disso, estes novos resultados, aproximam-se dos resultados obtidos com base em dados de satélite no período de tempo antes do incêndio. Na maior parte dos casos, a inclusão de G é relevante para que os resultados obtidos sejam compatíveis com os resultados obtidos com dados de satélite. Em geral, não há um sinal significativo do incêndio na série temporal dos dados modelados. Apenas num dos casos se observa um aumento da radiação total que parece resultar do aumento de G, mas deve novamente notar-se que tal se pode dever ao facto de G ter sido calculado com dados de satélite e não pelo modelo. Isto, porque como já referido, a LST obtida pelos dados de satélite mostra um aumento muito mais significativo que o observado nos dados de TSK provenientes do modelo SEB.

Os resultados dos dados de satélite são consistentes com os resultados observados em estudos anteriores e mostram a relevância que a LST tem nas anomalias observadas no balanço radiativo à superfície. Por outro lado, os resultados obtidos com o modelo SEB apresentaram algumas discrepâncias quando comparados com os resultados obtidos com dados de satélite, representando mal o comportamento do solo depois da ocorrência de um incêndio. Pôde-se também observar que, desprezando o G, os resultados perdem qualidade e, por isso, G é uma variável relevante para o estudo realizado. Este resultado mostra que seria importante que o conjunto de dados disseminados pela LSA-SAF incluísse os valores de G. Os resultados do modelo poderiam também ser melhorados, caso a TSK obtida fosse mais consistente com a LST detetada remotamente; para isso em vez de recorrer a valores estáticos da fração de cobertura vegetal, seria vantajoso utilizar valores diários da fração de coberto vegetal.

Palavras-chave

Incêndios Rurais, Deteção Remota, Balanço de Energia à Superfície, Temperatura de Superfície do Solo, Fluxos de Calor à Superfície

Index

List of Figures

List of Tables

List of Abbreviations

AL	Surface Albedo
ATBD	Algorithm Theoretical Basis Document
BB	Burned
BRDF	Bidirectional Reflectance Distribution Function
DSLF	Downward Surface Longwave Flux
DSSF	Downward Surface Shortwave Flux
ECMWF	European Center for Medium-range Weather Forecast
EPS	EUMETSAT Polar System
ET	Evapotranspiration
FVC	Fraction of Vegetation Cover
G	Soil Heat Flux
H	Sensible Heat Flux
H-TESSEL	Tiled ECMWF Scheme for Surface Exchanges over Land with revised hydrology
ICNF	*Instituto da Conservação da Natureza e das Florestas*
IGBP	International Geosphere–Biosphere Program
LAI	Leaf Area Index
LE	Latent Heat Flux
LSA-SAF	Satellite Application Facility on Land Surface Analysis
LST	Land Surface Temperature
LW	Longwave Radiation
MITECO	*Ministerio para la Transición Ecológica y el Reto Demográfico*
MODIS	Moderate Resolution Imaging Spectroradiometer
MSG	Meteosat Second Generation

NASA	National Aeronautics and Space Administration
NPP	National Polar-orbiting Partnership
NOOA	National Oceanic and Atmospheric Administration
NWP	Numerical Weather Prediction
SEB	Surface Energy Balance
SEVIRI	Spinning Enhanced Visible and Infrared Imager
SW	Shortwave Radiation
TOA	Top-of-the-Atmosphere
TSK	Skin Temperature
UB	Unburned
VCM	Vegetation Cover Method
VIIRS	Visible Infrared Imaging Radiometer Suite

1 Introduction

Wildfires play an important role on environmental change and land degradation in the Mediterranean basin (Quintano et al., 2015), a region that, in turn, is becoming more prone to the occurrence of large wildfires, as a result of climate change (Pausas, 2004), as well as of anthropogenic activities (San-Miguel-Ayanz et al., 2013). Mediterranean climate is characterized by mild and wet winters that favour the increase of fine fuels, followed by warm and dry summers that increase wildfire danger (Amraoui et al., 2013). Several authors have assessed the impact of climate and weather conditions on land surface, in particular on vegetation stress, by analysing surface parameters together with heat fluxes over periods and regions characterized by large fire activity (Amiro, 2001; Beringer et al., 2003; Chambers et al., 2005; Chambers & Chapin, 2003; Liu et al., 2018; Montes-Helu et al., 2009; Veraverbeke et al., 2012; Wendt et al., 2007). Although surface parameters like albedo (AL) and land surface temperature (LST) are commonly considered (Liu et al., 2018; Montes-Helu et al., 2009; Wendt et al., 2007), the same does not happen with net radiation that is modulated by both of them, as well as with longwave radiation (LW) and shortwave radiation (SW) balances. The aim of this work is therefore to study how fire events affect surface radiative fluxes and understand the impact wildfires have on the energy balance at the surface.

With that in mind, the first part of this work consists of the analysis of remotely sensed parameters over areas affected by wildfires. The increase in LST and decrease in AL after the occurrence of a fire is documented in different studies (Beringer et al., 2003; Chambers et al., 2005; Veraverbeke et al., 2012; Wendt et al., 2007; Silva, 2020). Vegetation reduction and ash deposition caused by the fire have immediate impacts on the properties and behaviour of the surface, as well as on sensible and latent heat fluxes (Rother & De Sales, 2020). If, in addition to these two parameters, the surface emissivity (EM), the downward surface shortwave flux (DSSF) and the downward longwave surface flux (DSLF) are studied, then it is possible to understand the change of net radiation, along with LW and SW balances. Therefore, the first part of this work aims at describing the changes in net radiation and LW and SW balances, as well as the changes in the parameters that contribute to these budgets, in a post-fire scenario. Satellite data are obtained from the Satellite Application Facility on Land Surface Analysis (LSA-SAF) as derived from observations performed by the Spinning Enhanced Visible and Infrared Imager (SEVIRI) onboard Meteosat Second Generation (MSG) satellites.

Besides the surface parameters already mentioned, another common way to study the impact of wildfires on the surface energy balance is, as previously stated, through the analysis of heat fluxes and the net radiation derived from them. For a tropical savanna in Australia, Wendt et al. (2007) showed that there is a reduction of surface albedo and subsequent increase of the energy that can be redirected into sensible and latent heat fluxes. The reduction of vegetation, which is burned in the fire, reduces the latent heat flux and causes an increase of the sensible heat flux. A decrease in albedo, as a result of the darkening of the soil and lower vegetation cover, leads to more energy being absorbed by the soil. This results in a significant increase of the ground heat flux after the fire. Beringer et al. (2003), again for a tropical savanna in Australia, obtained similar results, having found an increase in the sensible heat and in the ground heat fluxes, and a decrease in the latent heat flux after the fire. The increase in sensible and ground heat fluxes is clearly observed during the first 5 to 10 days after the fire. Furthermore, Quintano et al. (2015) and Rother & De Sales (2020) obtained results that are in accordance with the ones already mentioned. It has also been shown that the decrease in latent heat flux after a fire does not necessarily have to be significant. Along with this, it is worth noting that the burning of densely vegetated areas is associated with the decrease of sensible and latent heat fluxes while areas where vegetation is not as prominent are associated with increases in sensible heat fluxes (Rother & De Sales, 2020).

Taking this into account, the second part of this work's objective is to understand the change of sensible, latent, and ground heat fluxes and the resulting net radiation after a wildfire occurs. Data are obtained from a Surface Energy Balance (SEB) model constrained with LSA-SAF satellite data (Ghilain et al., 2011, 2012, 2016; Martins et al., 2019). This model estimates evapotranspiration, the sensible heat flux and latent heat flux.

A systematic comparison between diagnostic (first part) and model results (second part) provides a way of assessing the consistency among satellite derived data and validating the results computed with the SEB.

This work is divided into 5 chapters. Data and methods are described in Chapters 2 and 3. Results are presented in Chapter 4 which is divided into two parts, the first one respecting to diagnostic results, obtained directly from remotely sensed data, and the second one to the model results, obtained from data obtained using an algorithm applied by the LSA-SAF. Results are discussed in Chapter 5, and Chapter 6 presents the conclusion of this work.

2 Data

2.1. Satellite Data

Data analysed in this work were retrieved from the LSA-SAF site (https://landsaf.ipma.pt/), and cover the period from May to October 2020. Variables retrieved respect to products derived from SEVIRI/MSG observations and include: 1) Downward Surface Shortwave Flux – (MDSSF, product Id LSA-201), 2) Downward Surface Longwave Flux – (MDSLF, LSA-204), 3) Daily Surface Albedo – (MDAL, LSA-101), 4) Daily Land Surface Emissivity – (MEM, DEMO), 5) Land Surface Temperature – (MLST, LSA-001) and 6) Daily Leaf Area Index – (MDLAI, LSA-423).

2.1.1. Downward Surface Shortwave Flux

The downward surface shortwave flux (DSSF) quantifies the radiative energy that reaches the surface of the Earth, with wavelengths between 0.3 and 4.0 µm. This parameter heavily depends on the solar zenith angle, cloud cover and not as heavily on the atmospheric absorption and surface reflectivity. DSSF is computed from the three shortwave spectral bands of SEVIRI on board the MSG satellites, namely at 0.6 µm, 0.8 µm and 1.6 µm, at intervals of 30 minutes (Carrer et al., 2008). Given that DSSF has an inverse relationship with top of atmosphere (TOA) reflectance, albedo at TOA is the most important variable in the computation of DSSF. Depending on the sky conditions, whether it is clear or cloudy, different approaches are made to compute this parameter. If clear-sky conditions are verified, it is computed considering the effective transmittance of the atmosphere and the concentration of the atmospheric components. On the other hand, the approach used if clouds are present considers a cloud-atmosphere-surface system, where the values are computed based on a description of the radiative transfer (Trigo et al., 2011).

2.1.2. Downward Surface Longwave Flux

The downward surface longwave flux (DSLF) is the irradiance that reaches the surface in the infrared part of the spectrum, between 4 and 100 µm. This flux is computed from the Stefan-Boltzmann law and combines information from cloud, that is remotely sensed with SEVIRI/MSG, with temperature and humidity data from numerical weather prediction (NWP) models (Trigo et al., 2011). Input parameters emissivity and temperature are estimated as functions of the near-surface atmospheric temperature and/or water vapor content and atmospheric corrections are performed, e.g. by means of correcting factors based on cloudiness (Trigo et al., 2010). As in the case of DSSF, data are available every 30 minutes. DSLF data, as well as DSSF, are validated through comparison with *in situ* measurements (Trigo et al., 2011).

2.1.3. Surface Albedo

Surface albedo, hereafter albedo (AL), is defined as the ratio between the radiation that is reflected by the Earth's surface and the total radiation incident on the surface. It measures the fraction of radiation that is reflected by the surface (Carrer et al., 2018). The product used is disseminated on a daily basis, and is computed from the spectral bands of SEVIRI/MSG: in the visible at 0.6 µm, near infrared at 0.8 µm and shortwave infrared at 1.6 µm (Carrer et al., 2010). Satellite observations of reflectance are made at TOA level and atmospheric corrections are made to obtain reflectance at top of canopy (TOC) level, where albedo is computed. TOC reflectances are then used to estimate the bidirectional reflectance distribution function (BRDF), which is then angularly integrated to obtain the surface albedo (Carrer et al., 2018). The main causes of degradation of albedo data are persistent cloud

cover, high loads of aerosols in the atmosphere and recent changes of snow concentration. None of these situations are verified for the areas studied (Trigo et al., 2011).

2.1.4. Surface Emissivity

Surface emissivity is the ratio between the energy emitted by the body analysed and the energy emitted by a black body (body that emits/reflects all the energy incident on it) at the same temperature (Miyanishi, 2001). Emissivity is estimated for the SEVIRI channels centred at 3.9 μm, 8.7 μm, 10.8 μm and 12.0 μm. Broadband emissivity for the spectral range 3-14 μm is also estimated. The emissivity is computed considering that the total emissivity is the sum of the emissivity over the vegetation fraction and the land fraction for each pixel. This fraction is determined for each pixel using the daily Fraction of Vegetation Cover (FVC), a parameter also computed by the LSA-SAF. For each type of land cover, as obtained from the IGBP database, the respective emissivity has a weight according to the daily FVC. This computation does not consider reflectance between canopies and between canopies and the ground, so an uncertainty associated with each value is also computed. This uncertainty depends on the SEVIRI channel and on land cover type (Martins et al., 2019; Trigo, Peres, et al., 2008).

2.1.5. Land Surface Temperature

Land Surface Temperature (LST) LST is defined as the directional radiometric temperature measured at the surface, constrained to the sensor's field of view (Ermida et al., 2014; Norman & Becker, 1995). LST is the best approximation to the thermodynamic temperature of the surface (Trigo et al., 2011), and has an important role in the long-wave radiation emitted by the Earth's surface as well as in the surface heat fluxes (Trigo, Monteiro, et al., 2008).

LST is computed every 15 minutes using the Generalized Split Window (GSW) algorithm (Freitas et al., 2010) that relies on SEVIRI/MSG measurements of clear-sky TOA brightness temperatures of split-window channels centred at 10.8 mm and 12.0 mm. Because of the high temporal resolution, data retrieved by geostationary satellites like MSG allow describing the daily cycle of LST (Trigo, Monteiro, et al., 2008). Validation of LST is performed by comparing retrieved values with *in situ* measurements, as well as with other measurements from different instruments on-board other satellites (Ermida et al., 2014; Trigo et al., 2021).

2.1.6. Leaf Area Index

Leaf Area Index (LAI) relates to the amount of green leaf material that is alive and is observed in the canopy. LAI is defined as one half of the total leaf area per unit ground area (Trigo et al., 2011). LAI is estimated from the fraction of vegetation cover (FVC) (Trigo et al., 2011) through a semi-empirical process (Roujean & Lacaze, 2002). LAI is estimated using the DISMA (Directional Spectral Mixture Analysis Method) that relies on retrieved data from SEVIRI/MSG is used from channels centred at 0.6 μm, 0.8 μm and 1.6 μm. LAI is computed on cloud-free pixels and correction is performed for atmospheric effects. Results are influenced by canopy structure, the reflectance from the surface under the canopy and the mean single-scattering albedo, and the validation is performed against *in situ* measurements (García-haro et al., 2006).

2.2. Surface Energy Balance Model

In order to estimate evapotranspiration, the LSA-SAF uses a Surface Energy Balance (SEB) model applied to the area covered by SEVIRI/MSG (Ghilain et al., 2011). The algorithm is based on the surface scheme used operationally by the European Center for Medium-range Weather Forecast (ECMWF), namely the Tiled ECMWF Scheme for Surface Exchanges over Land with revised

hydrology (H-TESSEL) (Albergel et al., 2012; Balsamo et al., 2009; Van den Hurk et al., 2000; Viterbo & Beljaars, 1995). The algorithm makes use of remote-sensing data (mainly from MSG/SEVIRI), including surface albedo, leaf area index, incoming radiation fluxes, and soil moisture. Algorithm inputs that are not available as satellite products are obtained from global numerical weather forecasts (ECMWF).

The algorithm that solves the SEB to estimate evapotranspiration is the LSA-SAF ET v2 algorithm, and a full description is available in the Algorithm Theoretical Basis Document (ATBD) of the product (Ghilain, 2016).

The algorithm considers each SEVIRI/MSG pixel as a sum of *i* tiles, that are categorized by their land cover types. The fraction of each tile in the SEVIRI/MSG pixel is estimated based on the land cover map from the ECOCLIMAP database (Ghilain et al., 2012). To obtain evapotranspiration, the algorithm considers the partition of net radiation ($R_{N-flux,i}$) into sensible heat flux (H_i), latent heat flux (LE_i) and ground heat flux (G_i). Net radiation is portioned as follows:

$$R_{N-flux,i} = H_i + LE_i + G_i \tag{2.1}$$

Net radiation ($R_{N,i}$) can also be obtained from the balance between shortwave and longwave radiation:

$$R_{N,i} = (1-\alpha)S_{\downarrow} + \varepsilon\left(L_{\downarrow} - \sigma T_{sk,i}^4\right) \tag{2.2}$$

where α is the surface albedo, $S_{\downarrow}$ the downward surface shortwave flux, ε the surface emissivity, $L_{\downarrow}$ the downward surface longwave flux, σ the Stefan-Boltzmann constant and T_{sk} the skin temperature. All variables refer to each pixel and, except the T_{sk} that is estimated by the model, they consist of inputs computed from satellite data.

In equation 2.1, the ground heat flux (G_i) is the rate of heat storage in the soil and vegetation as a result of conduction (Huang et al., 2013). It is approximated as:

$$G_i = \beta_i * R_{N,i} \tag{2.3}$$

where

$$\beta_i = 0.5 * exp(-2.13 * (0.88 - 1.78 * exp(-0.6\, LAI_i))) \tag{2.4}$$

and where subscript *i* refers to the i-th tile.

Computations of sensible heat flux (H), associated with the exchange of heat by convection, and of latent heat flux (LE), related with the exchange of heat when there is a change of state in water, are performed using a resistance approach that combines two effects: the response of the stomata closure related with stress caused by the environment, which is modelled by the canopy resistance (r_c); and the aerodynamic resistance (r_a). Moreover, canopy resistance depends on minimum stomatal resistance, LAI, $S_{\downarrow}$, unfrozen soil water content, atmospheric water pressure deficit and plant characteristics; and aerodynamic resistance depends on the stability of the atmosphere and the intensity of turbulence (Martins et al., 2019). Using this approach, estimates of H are obtained as:

$$H_i = \frac{\rho_a}{r_{a_i}}\left[c_p\left(T_{sk,i} - T_a\right) - g z_a\right] \tag{2.5}$$

where ρ_a is the air density, c_p is the specific heat capacity, T_a the air temperature measured at 2 m, g the gravitational acceleration and z_a the air temperature measurement height (2 m).

Estimates of LE are in turn obtained as:

$$LE_i = \frac{L_v \rho_a}{(r_{a_i} + r_{c_i})}\left[q_{sat}(T_{sk,i}) - q_a(T_a)\right] \quad (2.6)$$

where L_v is the latent heat of vaporization, q_{sat} the specific humidity at saturation and q_a the specific humidity. Except for T_{sk}, all parameters are estimated from numerical weather prediction data or/and satellite data (more details are provided in the ATBD).

Skin temperature (T_{sk}), sensible (H) and latent (LE) heat fluxes are estimated through an iterative process applied to SEB, which runs until stability is reached. For T_{sk}, stability is attained when two consecutive iterations have a difference smaller than 0.01 and for H and LE, the iterative process is considered stable when results of two consecutive iterations have a difference smaller than 0.1. The model stops after 100 iterations if convergence is not verified. Results obtained through this algorithm were verified against several *in situ* observations over Europe and Africa.

Evapotranspiration (ET) is a bio geophysical parameter that quantifies the amount of water lost through evaporation from the soil or from the surface vegetation or from transpiration through the leaves (Kunkel, 2001; Trigo et al., 2011). It is computed from the LE as:

$$ET = 3600\frac{LE}{L_v} \quad (2.7)$$

where L_v is the latent heat of vaporization. Values of ET are available every 30-minute (with units $mm.h^{-1}$), which are then converted to mm considering the integration period of 30-minutes.

The LSA-SAF SEB model only disseminates the outputs of evapotranspiration (MET, product Id LSA-311), sensible heat flux (MH, LSA-304) and latent heat flux (MLE, LSA-305). To obtain the net radiation as estimated by the SEB model, the ground heat flux, G, was also estimated following equation (2.3) and using the LAI product. The corresponding net radiation (R_{N-flux}) was then estimated from equation (2.1).

3 Methodology

3.1. Selection of fire scars

Five burned areas were selected using maps kindly supplied by Miguel Mota Pinto, who used a deep learning approach to identify burned scars using temporal sequences of satellite images acquired by the Visible Infrared Imaging Radiometer Suite (VIIRS) instrument aboard the joint NASA/NOAA Suomi National Polar-orbiting Partnership (Suomi NPP) and NOAA-20 satellites (Pinto et al., 2020). These areas were selected based on the extent of burned areas, and respectively data available, especially around the time when the fire event took place. The selected wildfire episodes were those that occurred in Budens, Oleiros, Huelva, Covilhã and Castro Verde in the year of 2020. Further details about are provided in Table 3.1, that shows for each event the area burned, and the starting and ending date as derived from satellite observations.

Table 3.1 - Chosen fire scars description. Localization, start and end date and burned area are shown. Area burned retrieved from ICNF and MITECO.

Wildfire	Start date	End date	Area burned (ha)
Budens	19 june 2020	21 june 2020	2303
Oleiros	26 july 2020	27 july 2020	5590
Huelva	27 august 2020	31 august 2020	12101
Covilhã	30 july 2020	31 july 2020	1084
Castro Verde	14 july 2020	15 july 2020	2382

For each fire scar, VIIRS-based maps of burned area were then used to estimate the fraction of burned area in each coarser scale SEVIRI pixel. Pixels with high burned fraction were selected as burned (BB) pixels. Sets of unburned (UB) pixels were also selected considering the landcover similarity to the burned ones. Information on landcover was obtained from the Copernicus CORINE dataset of 2018, which was analysed through the Google Earth Engine (GEE) platform (Gorelick et al., 2017). It is worth mentioning that, for each fire event, the number of selected UB pixels is the as of BB pixels (and with similar land cover type). The fraction of burned area in each SEVIRI pixel for each fire scar, as well as the sets of selected BB and UB pixels are shown in Figure 3.1. Satellite data (as described in section 2.1) were then extracted for each of the selected pixels. For scars with more than 1 pixel selected for BB/UB, the mean of data for the BB/UB pixels is computed.

3.2. Net radiation computation

The impact of fires events on net radiation (R_N) was first analysed by considering the available satellite data. As such, a satellite-based estimate of R_N was first derived using equation (2.2), and using the satellite products DSSF, DSLF, AL, EM and LST. The main difference to the SEB-estimated R_N is that this approach makes use of the LST retrieved from satellite observations. For each fire scar, the shortwave balance ($R_{SW} = (1 - \alpha)S_{\downarrow}$) and longwave balance ($R_{LW} = \varepsilon(L_{\downarrow} - \sigma T_{LST}^4)$) are also analysed independently.

Following Wang et al. (2005), the broad-band emissivity of equation (3.1), that corresponds to the spectral range 3-25 μm, was obtained from SEVIRI channel emissivities at 8.7 μm ($\varepsilon_{8.7}$), 10.8 μm ($\varepsilon_{10.8}$) and 12.0 μm ($\varepsilon_{12.0}$):

$$\varepsilon_{3-25} = \frac{(14-3)\,\varepsilon_{3-14} + (25-14)\varepsilon_{14-25}}{(14-3)+(25-14)} \tag{3.1}$$

with

$$\varepsilon_{3-14} = a * \varepsilon_{8.7} + b * \varepsilon_{10.8} + c * \varepsilon_{12.0} \tag{3.2}$$

and where a, b and c are coefficients taking the values 0.1828, 0.3867 and 0.4395, respectively. Emissivity ε_{3-25} will be the one considered in the computation of R_N through the available satellite data.

In this study, only data between 12h and 14h30 UTC will be analysed since they are very likely to include the daily maximum of LST. Since the LST product does not provide data under cloudy conditions only clear-sky data are analysed. To be comparable to the variables of the SEB model that are all-sky, it is necessary to restrict the data to days with enough clear-sky data. The criteria chosen was that days with valid data were those with more than 70% of LST data retrieved in the period selected (12h to 14h30). The adopted criterion is a compromise between data being representative of clear-sky and having enough data for the analysis. For LST (computed every 15-minutes), DSLF, DSSF, H, LE and ET (computed every 30-minutes), a daily value is considered as the mean for each variable for the interval from 12h to 14h30.

To reduce the impact of erroneous values in the products that might obscure the signal of the burned scar, a smoothing of the data is carried out prior to the analysis. All variables considered in this study, are therefore moving medians for ±5 days around the considered day, e.g. the value attributed to day 6 is computed as a median from day 1 to day 11. Moreover, data are classified as valid if at least 6 days were considered valid after the clear-sky filtering described in the previous section.

The period analysed is from May to October 2020. The reason is because data from January to May and from November and December have a large number of missing values. However, the period studied is long enough to contain the main variability of the different variables and of the vegetation recovery after the fire.

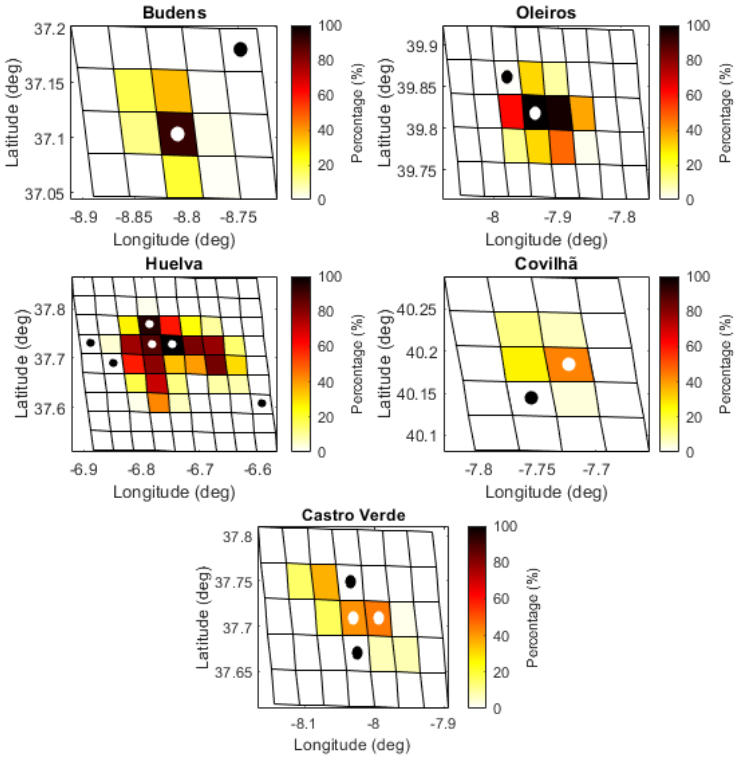

Figure 3.1 - Burned fraction in each pixel for all fire scars selected. White dots and black circles mark selected burned (BB) and unburned (UB) pixels, respectively.

4 Results

4.1. Diagnostic results

4.1.1. Downward Surface Shortwave Flux

Figure 4.1 shows time series for the period studied of averaged DSSF for BB and UB pixels and the difference between those averages (BB minus UB). The natural seasonal cycle is clear for all the studied areas, with maximum values occurring during the summer months (June and July). There are small fluctuations in all cases but, as expected, no major differences are found between BB and UB pixels. The main exception is the case of Huelva where there is a decrease of the DSSF in BB pixels compared to UB ones. This may be attributed to a large fire plum spreading south (which does not impact the selected unburned pixels) that is clearly seen on Aqua/MODIS visible reflectance imagery on the 29th of August (obtained through NASA Worldview, Figure 4.2). There are also large differences observed in the Budens case, close to the end of October. In this case, the differences seem to be related to broken clouds.

4.1.2. Downward Surface Longwave Flux

Averaged DSLF for BB and UB pixels for the period studied and the respective differences are shown in Figure 4.3. As expected, there are small fluctuations in all cases, but there are no significant differences in DSLF between BB and UB pixels namely after the fire starts. In the case of Oleiros and Covilhã, there seems to be a persistent difference between the BB and UB pixels. Since most inputs of the DSLF algorithm come from numerical weather prediction, the source of this difference is not clear. The seasonal cycle can be seen in all cases even though it is not very accentuated: maxima can be observed in the summer, followed by a steady decrease towards the end of the year.

4.1.3. Albedo

Figure 4.4 shows time series of averaged AL for BB and UB pixels for the period studied, and of differences between BB and UB. In all cases, and more prominently in the case of Oleiros and Huelva, there is a decrease in AL right after the fire. This is consistent with a decrease in the vegetation density and the presence of charred material. The maximum difference in AL observed after the fire is in Huelva and Oleiros, that reaches about 0.02. For the cases of Covilhã and Castro Verde, the differences are smaller than the previous ones but still noticeable, while in the case of Budens, the difference is not so conspicuous. AL anomalies seem to increase with increasing fraction of burned area.

Steady increases in AL after the fire are also apparent (during 1-2 months), which are related to a decrease in the presence of char and ash on the surface (typically dispersed by the wind and/or rain) and development of short vegetation (Bremer & Ham, 1999; Pausas & Vallejo, 1999; Tsuyuzaki et al., 2009).

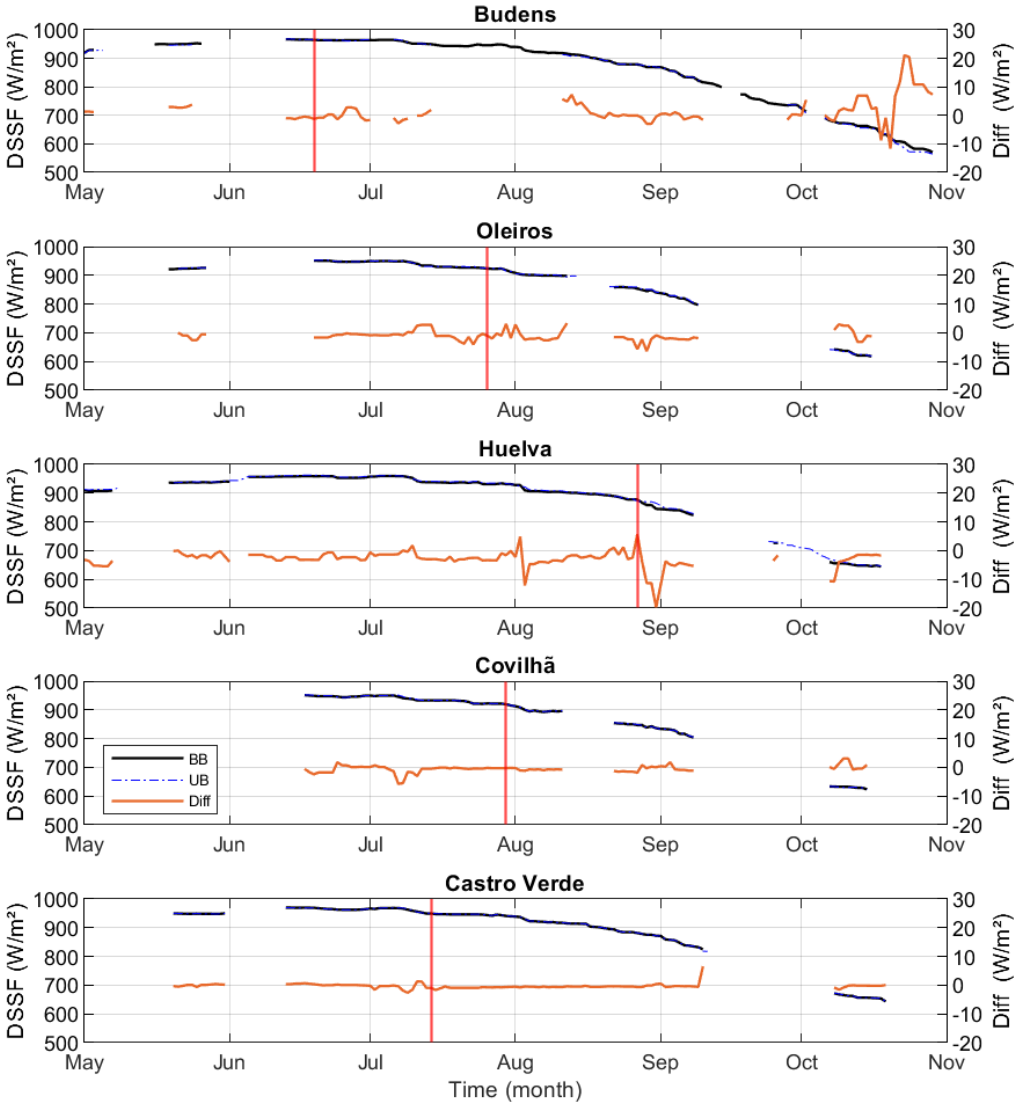

Figure 4.1 - Downward Surface Shortwave Flux (DSSF) from May to October 2020 for all studied events. Solid black and blue dash point lines, respectively, represent time series of DSSF for BB and UB pixels, respectively, whereas the solid orange lines represent time series of the differences of DSSF between BB and UB pixels (BB-UB) and respective differences between DSSF for BB and UB pixels. Left y-axis and right y-axis are for DSSF and DSSF differences, respectively. The vertical red lines identify the starting dates of the wildfire events.

Figure 4.2 - Analysis of Aqua/MODIS visible reflectance imagery on the 29th of August covering the region of Huelva. Source: NASA Worldview.

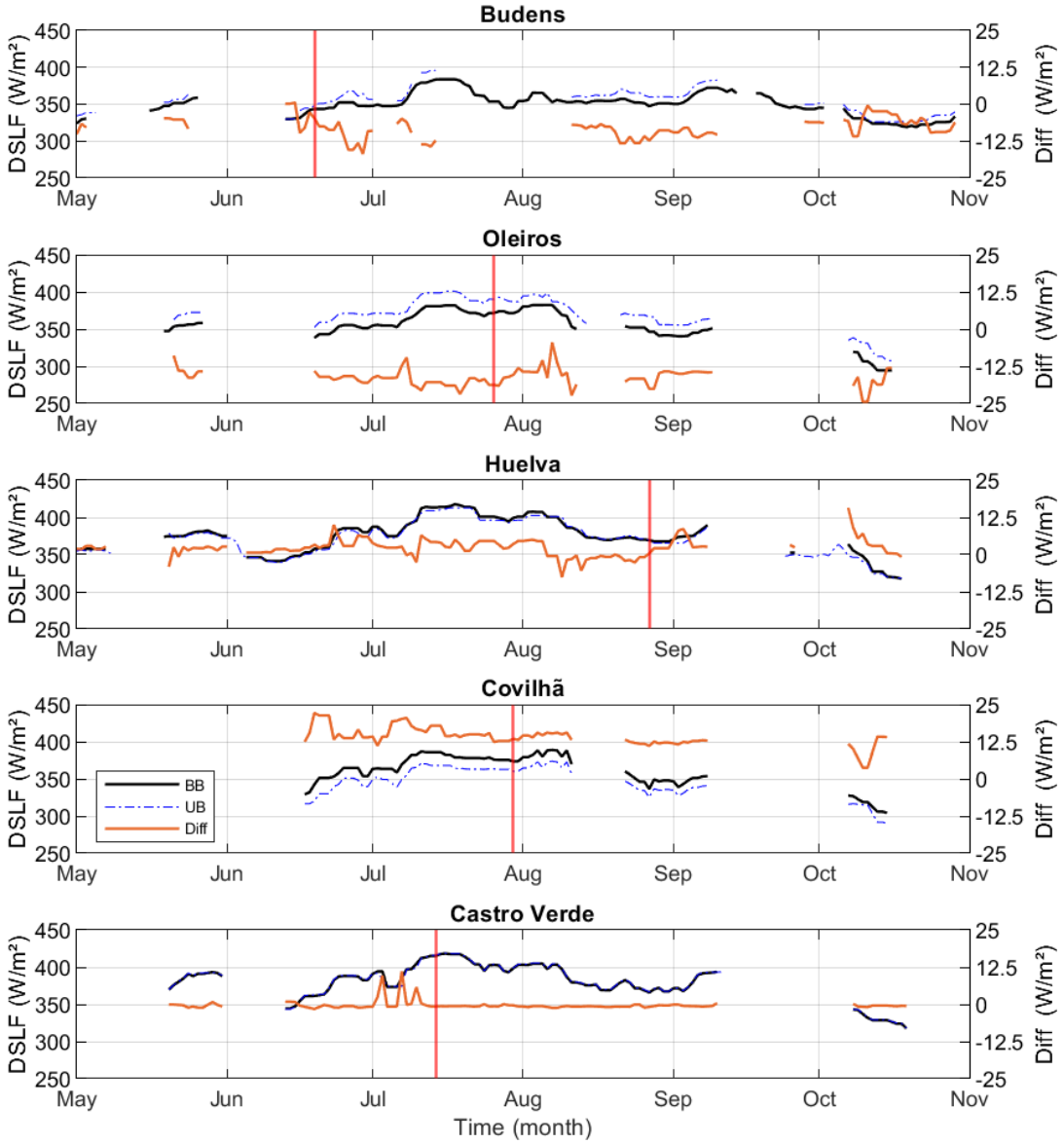

Figure 4.3 - As in Figure 4.1 but for Downward Surface Longwave Flux (DSLF).

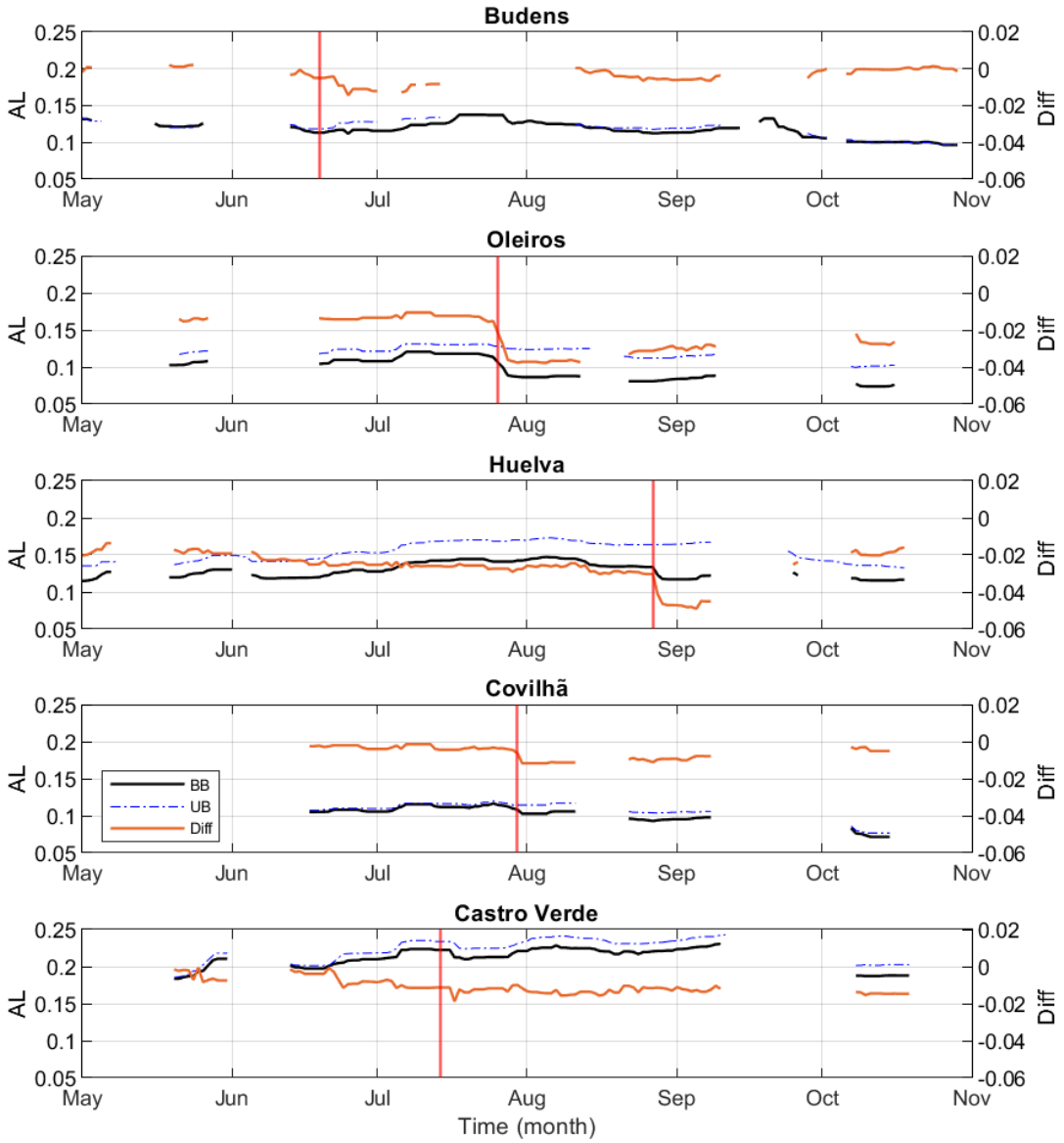

Figure 4.4 - As in Figure 4.1 but for Surface Albedo (AL).

4.1.4. Emissivity

Emissivity is a parameter that depends on soil properties, and therefore changes are to be expected after a wildfire event. Figure 4.5 shows time series for the period analysed of averaged EM for BB and UB pixels, as well as the difference between both. There is a marked decrease in emissivity right after the fire in the cases of Budens, Oleiros and Huelva. For Covilhã, a small decrease is also observed while for Castro Verde no major change is detected. For the Budens and Huelva cases, the differences in EM before and after the fire are as high as 0.004. The case where the difference registered after the fire is the largest takes place in Oleiros, where the difference is about 0.008. For the period considered (May to October), the fingerprint of vegetation recovery in EM is not evident.

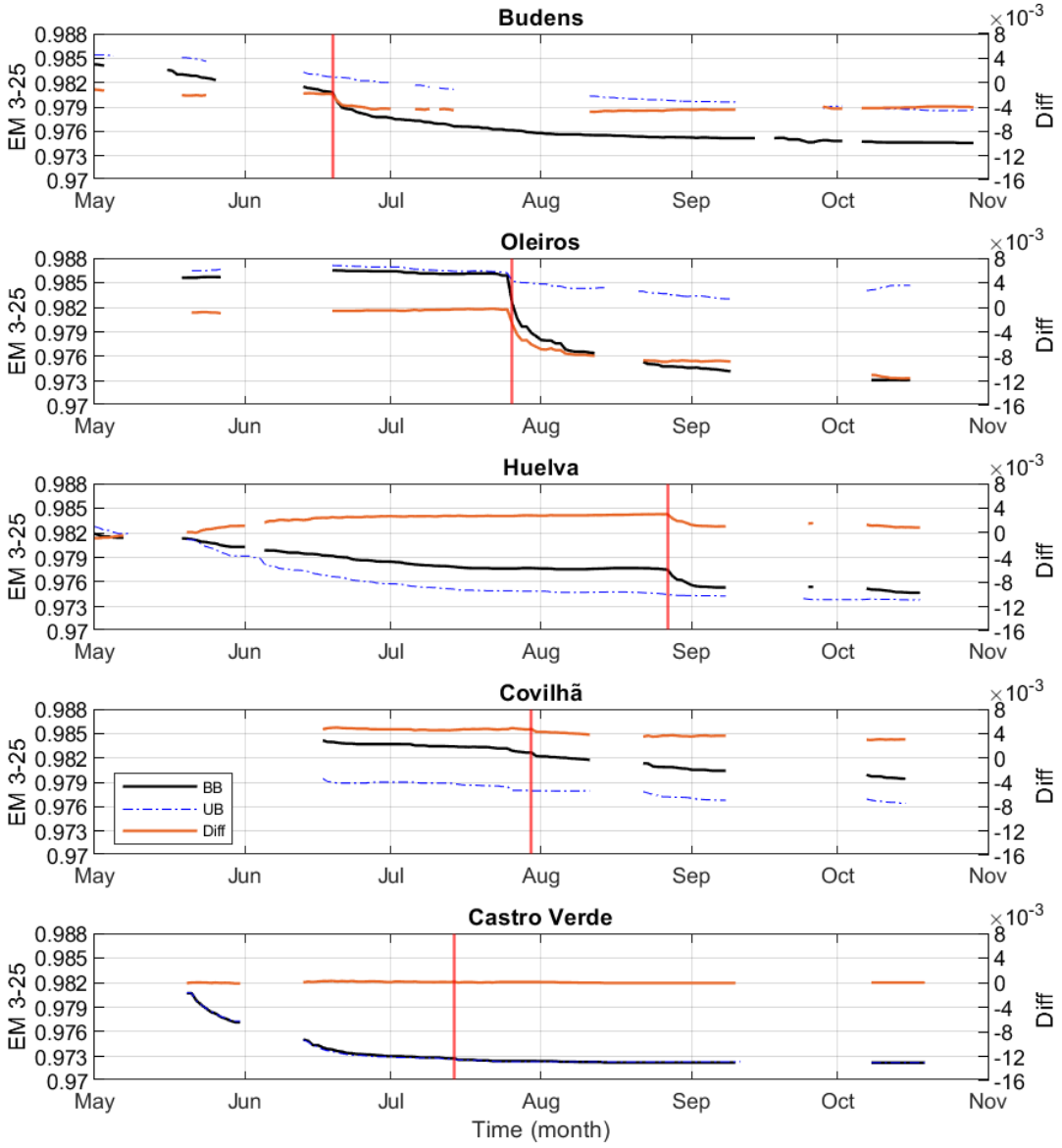

Figure 4.5 - As in Figure 4.1 but for Broadband Emissivity (EM).

4.1.5. Land Surface Temperature

Time series of averaged Land Surface Temperature for BB and UB pixels and of their differences are shown in Figure 4.6. Since LST is affected by both surface and atmospheric conditions, the impact of the fire scar may be difficult to assess given the high spatial and temporal variability of the LST. However, in all cases, an increase in LST in the BB pixels right after the fire can be observed. In the case of Castro Verde, the LST anomaly seems to start before the fire, which is likely an artifact due to the use of a moving median on time-series (see section 3.2). The maximum difference is about $5°C$ for Budens, $10°C$ for Oleiros and Huelva, and 3℃ and 1.5℃ for Covilhã and Castro Verde. The observed increase in LST is consistent with a decrease in vegetation density, and has been previously reported in other studies (Liu et al., 2018; Montes-Helu et al., 2009; Veraverbeke et al., 2012; Wendt et al., 2007; Silva, 2020).

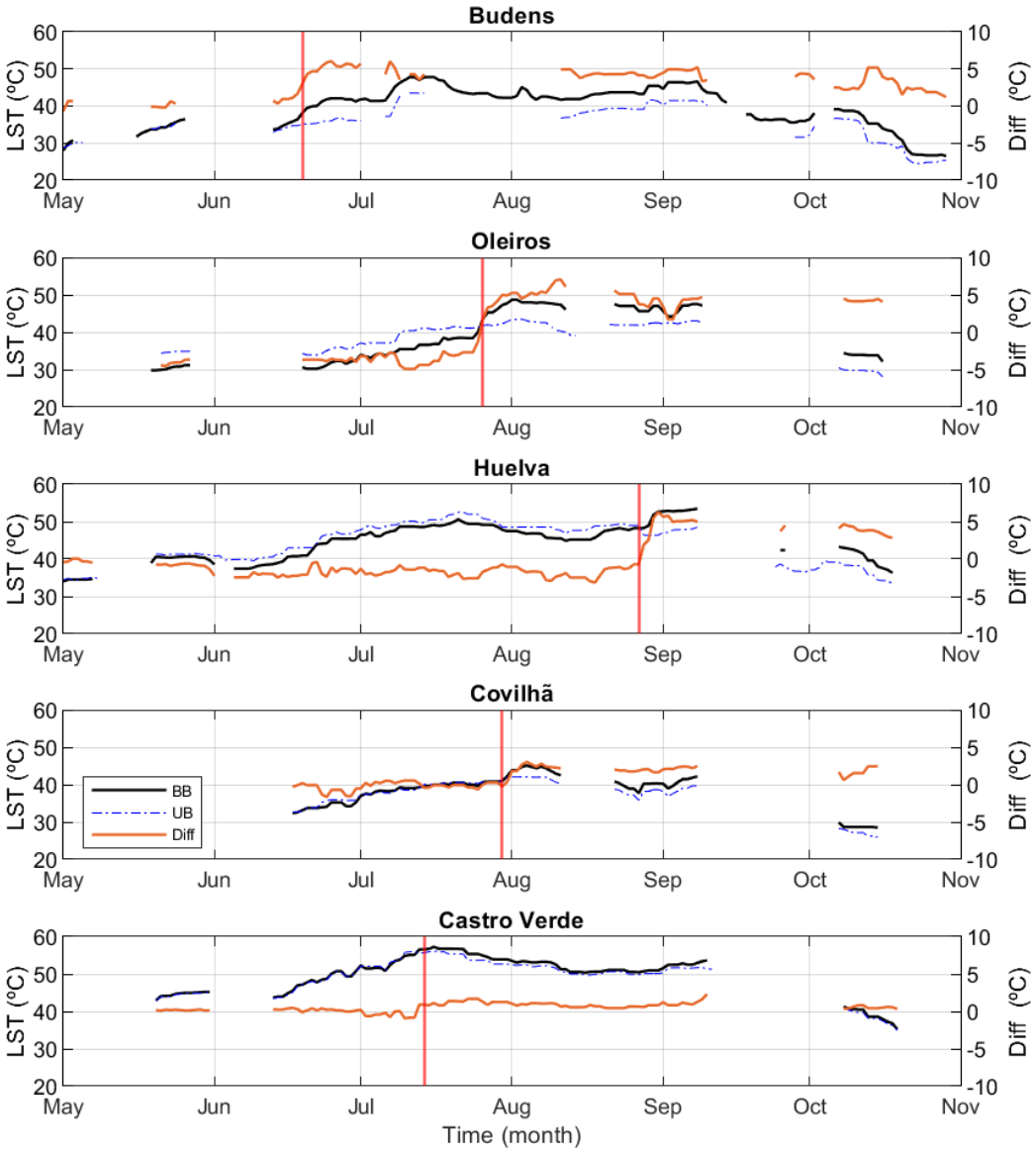

Figure 4.6 - As in Figure 4.1 but for Land Surface Temperature (LST).

4.1.6. Shortwave Radiation Balance

Time series of averaged shortwave radiation (SW) balance in BB and UB pixels and their differences are shown in Figure 4.7. Given the low impact of fire scars on DSSF, SW balance anomalies are expected to be mainly controlled by AL anomalies. In most cases, there is a slight increase in SW radiation in the BB pixels, which is consistent with the observed decrease in albedo. The Huelva case is the only case with a marked increase in DSSF differences right after the fire. Because of this, the time-series of SW radiation at Huelva shows an increase right after the fire that is consistent with the albedo decrease, followed by a deep decrease resulting from the DSSF decrease, and followed again by an increase due to the reduction in the DSSF and albedo differences that are still present. The highest anomaly in SW balance is observed for the Oleiros fire, reaching a difference of around 25 Wm^{-2}, consistent with the highest albedo differences.

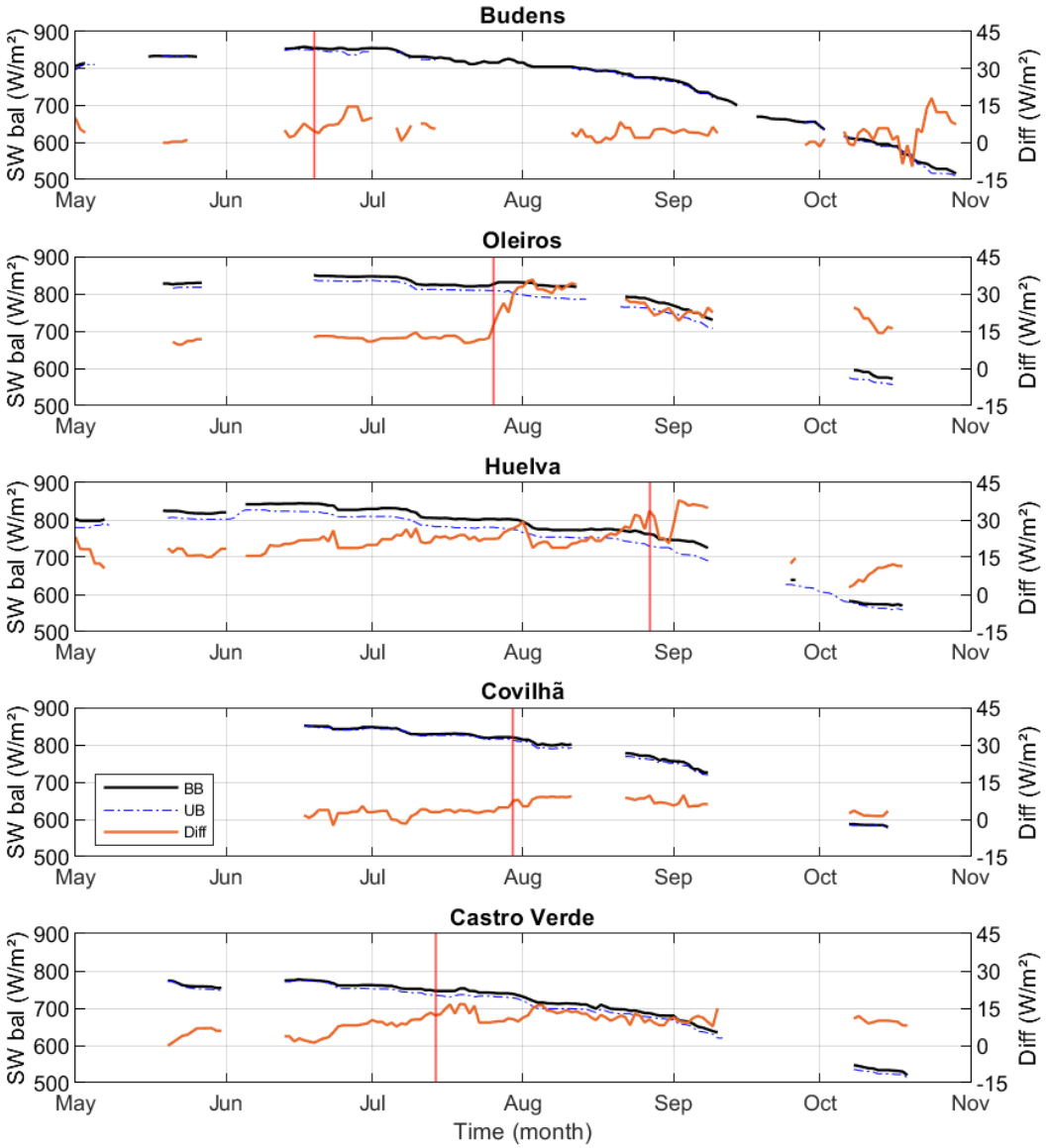

Figure 4.7 - As in Figure 4.1 but for Shortwave radiation balance (SW).

4.1.7. Longwave Radiation Balance

In the case of the Longwave radiation (LW) balance, since DSLF shows no significant response to the fire events, the major roles are played by EM and LST. Figure 4.8 shows time series of averaged LW balance for BB and UB pixels, and for differences between them. There is in general an absolute increase of LW leaving BB pixels after the fire in all areas studied. Castro Verde is the area where it is the most difficult to identify it since it has a smoother decrease. Budens, Oleiros and Huelva have higher increases in LW balance differences, reaching about 50 Wm^{-2} (Budens) and 60 Wm^{-2}(Oleiros and Huelva). Covilhã and Castro Verde show maximum differences of about 35 Wm^{-2} and 15 Wm^{-2}, respectively. The observed absolute increase in LW is consistent with the increase in LST, which also shows higher differences in Budens, Oleiros and Huelva. The impact of the emissivity on the LW is more difficult to assess since the corresponding channel estimates are also used to derive the LST.

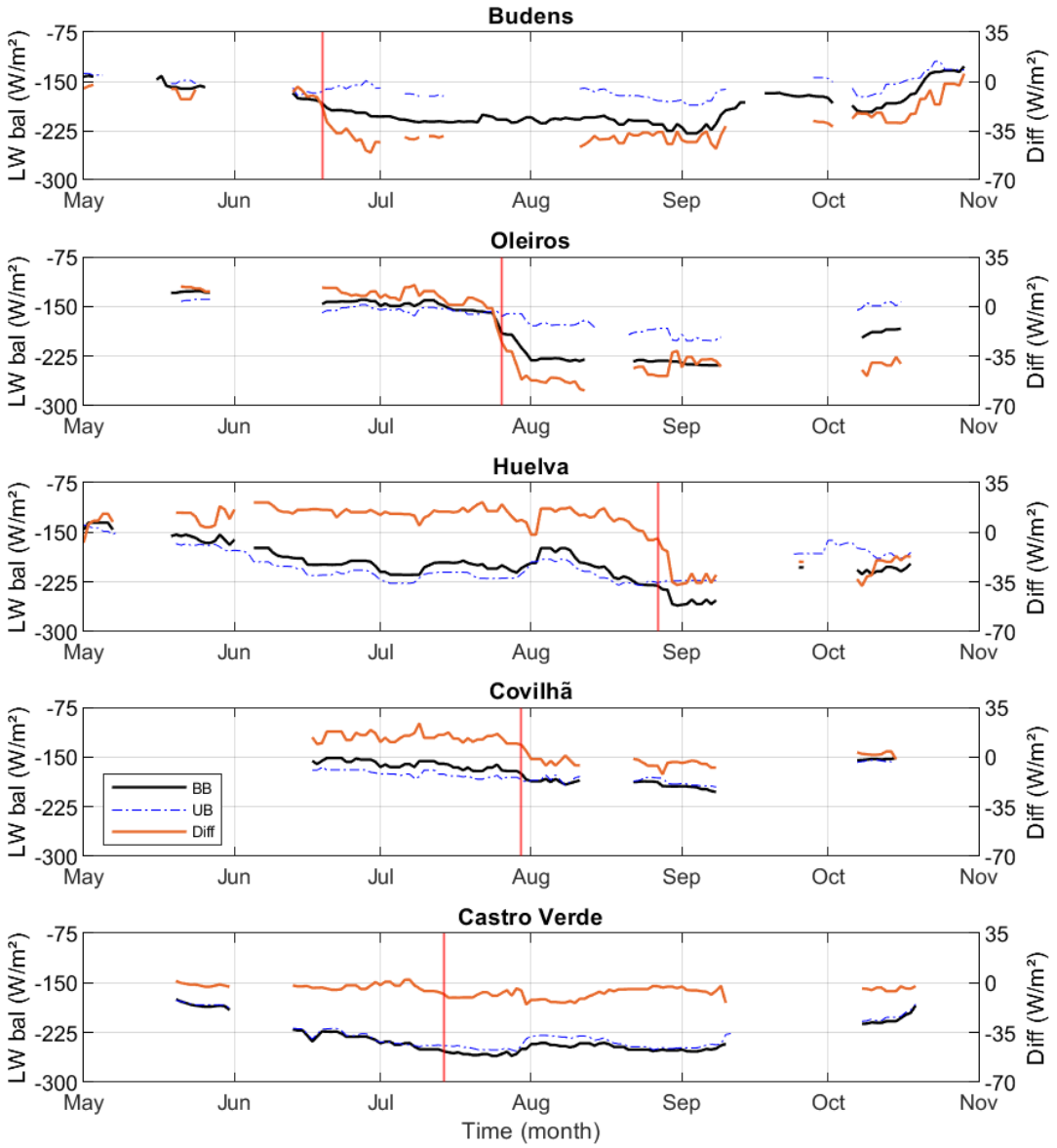

Figure 4.8 - As in Figure 4.1 but for Longwave radiation balance (LW).

4.1.8. Net Radiation

Figure 4.9 shows results for the net radiation (Net) that represents the balance between incoming SW and outgoing LW ($Net = SW + LW$). During summer, over mid-latitudes, values of Net are typically positive due to the higher incoming solar radiation. As discussed before, for BB pixels, there is a slight increase in the SW balance because less radiation is being reflected at the surface. The LW balance also increases in absolute values, which is associated to an increase in surface emitted radiation. For all cases except Castro Verde, the increase in outgoing LW is higher than the increase in SW being absorbed, resulting in a decrease of the net radiation after the fire. For the first four cases, the maximum absolute value of difference right after the fire is about 35 Wm^{-2} in Budens, 50 Wm^{-2} in Oleiros and Huelva and 15 Wm^{-2} in Covilhã.

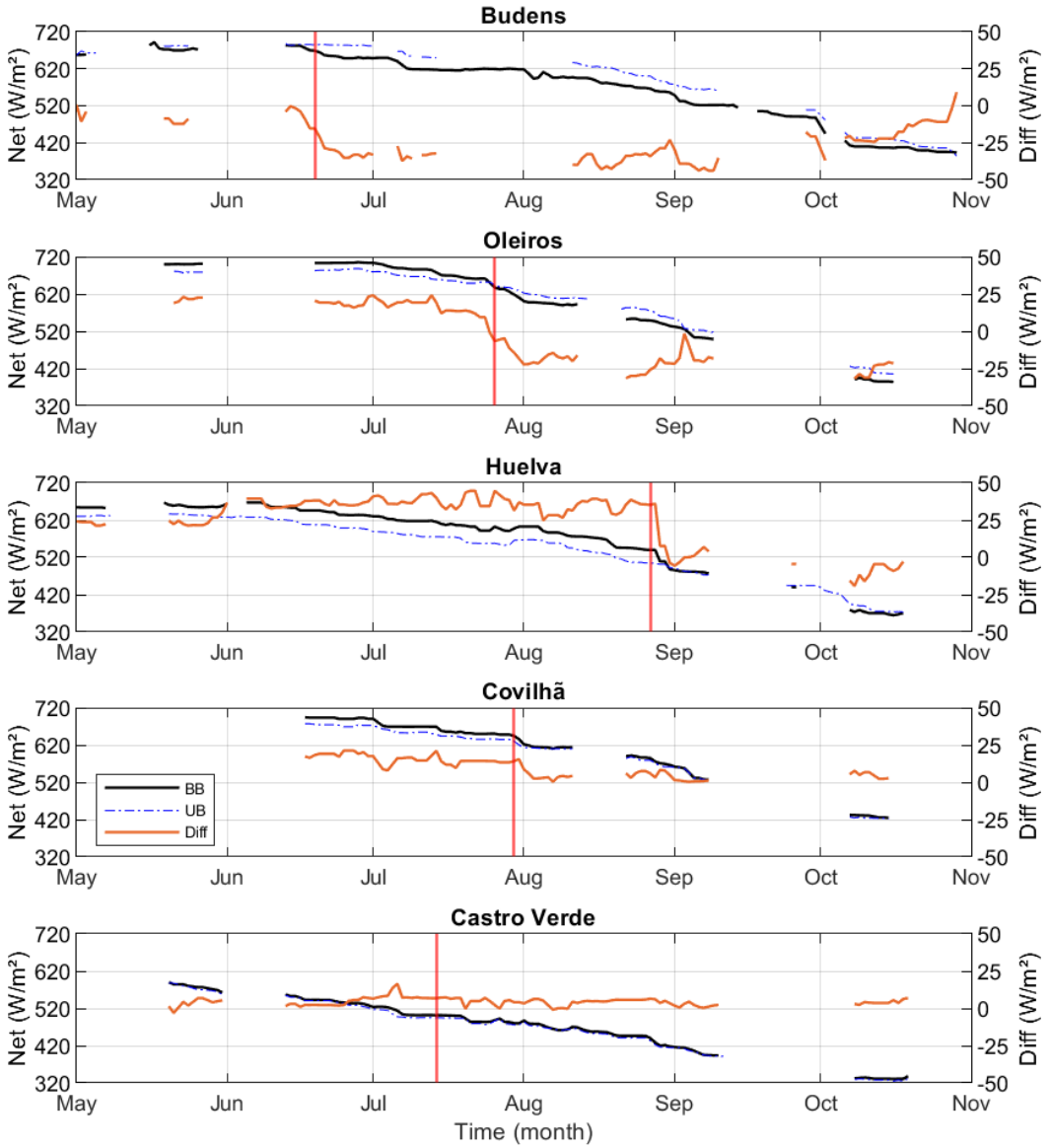

Figure 4.9 - As in Figure 4.1 bout for Net radiation (computed from retrieved data).

4.2. Model Results

4.2.1. Skin Temperature

Skin temperature (TSK), as discussed above, is the surface temperature as derived by the ET algorithm (which uses a SEB model). TSK is a critical variable in the partition between latent and heat fluxes and, therefore, it may be considered a diagnostic variable of the SEB model. In order to evaluate the quality of TSK estimates, LST (derived from satellite) may be used as reference. Figure 4.10 shows, for the period studied, time series of averaged TSK for BB and UB pixels and of their differences. An increase in TSK after the fire is observed for Oleiros and Huelva, but the increase is not as steep for Covilhã. In Budens, TSK varies in the opposite way right after the fire, while in Castro Verde no change is apparent. The increase right after the fire is best observed in Huelva. In this event, the difference of TSK is around 5℃, whereas in Oleiros this difference is about 2℃. Taking into account that the difference of LST for both these events is about 10℃, then the difference in TSK is at most half of the

one observed in LST. In all cases, the SEB model seems to underestimate surface temperature variations associated to fire events.

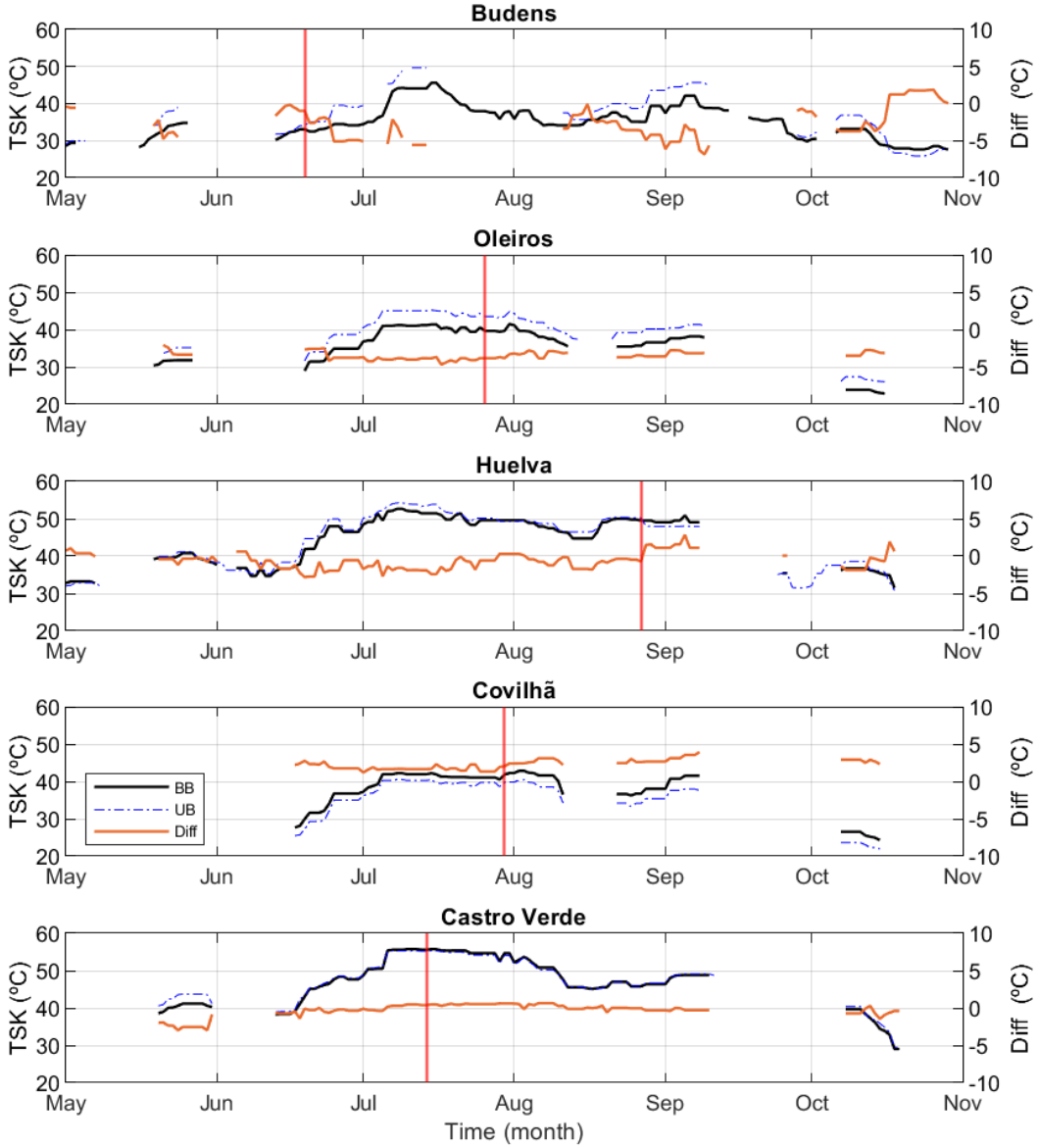

Figure 4.10 - As in Figure 4.1 but for Skin Temperature (TSK).

4.2.2. Evapotranspiration

Figure 4.11 shows time series of averaged evapotranspiration (ET) in BB and UB pixels and differences between them as estimated by the SEB model in the period analysed. After the fire, there is a small decrease in ET in BB pixels that is observed in most cases, which is best seen in Budens and Huelva. This decrease was expected considering that the occurrence of a fire causes a reduction of vegetation coverage, which should lead to a reduction of evapotranspiration in the areas affected.

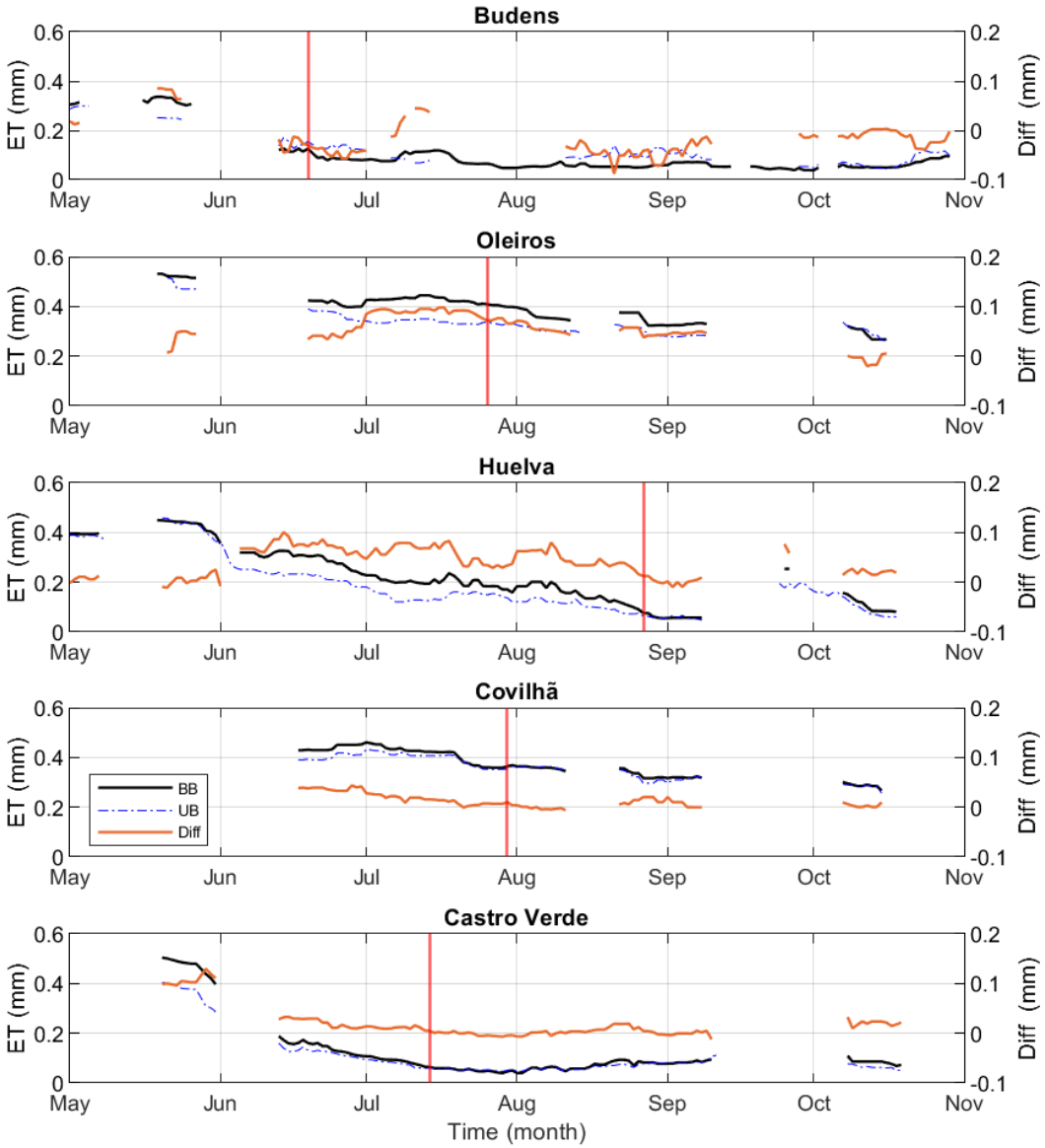

Figure 4.11 - As in Figure 4.1 but for Evapotranspiration (ET).

4.2.3. Sensible Heat Flux

Time-series of averaged sensible heat flux (H) over BB and UB pixels and of their differences, as estimated by the SEB model, are shown in Figure 4.12. Except for Budens, all remaining areas show an increase in the H difference after the fire. In the Budens event, there is a slight decrease right after the fire followed by an increase but, considering the noise in the series, one cannot be sure that it is due to the fire event. An increase of H is expected due to the increase in surface temperature (Wendt et al., 2007).

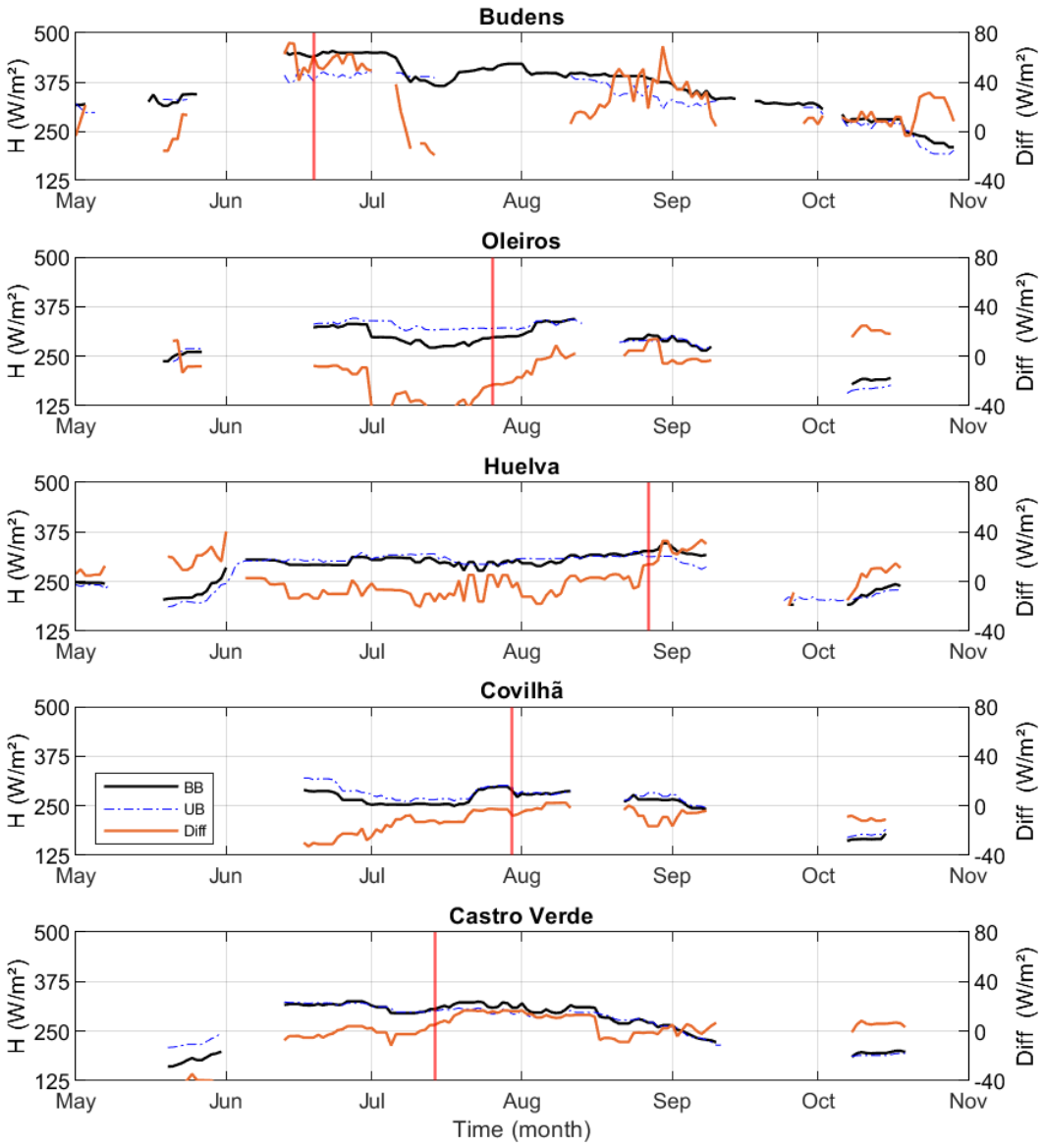

Figure 4.12 - As in Figure 4.1 but for Sensible Heat Flux (H).

4.2.4. Latent Heat Flux

Figure 4.13 presents time series of the SEB model estimates of averaged latent heat flux (LE) for BB and UB pixels and the respective differences. As shown in Equation (2.7), the evapotranspiration and the latent heat flux are co-dependent, as ET is computed from LE values. In all events, a small decrease in LE is observed (as for ET), and in Huelva this difference is more apparent than in the remaining areas. The latent heat flux is associated with water evaporation. Therefore, since soil moisture is very low during this time of the year, as vegetation is reduced so does evapotranspiration, leading to a decrease in LE.

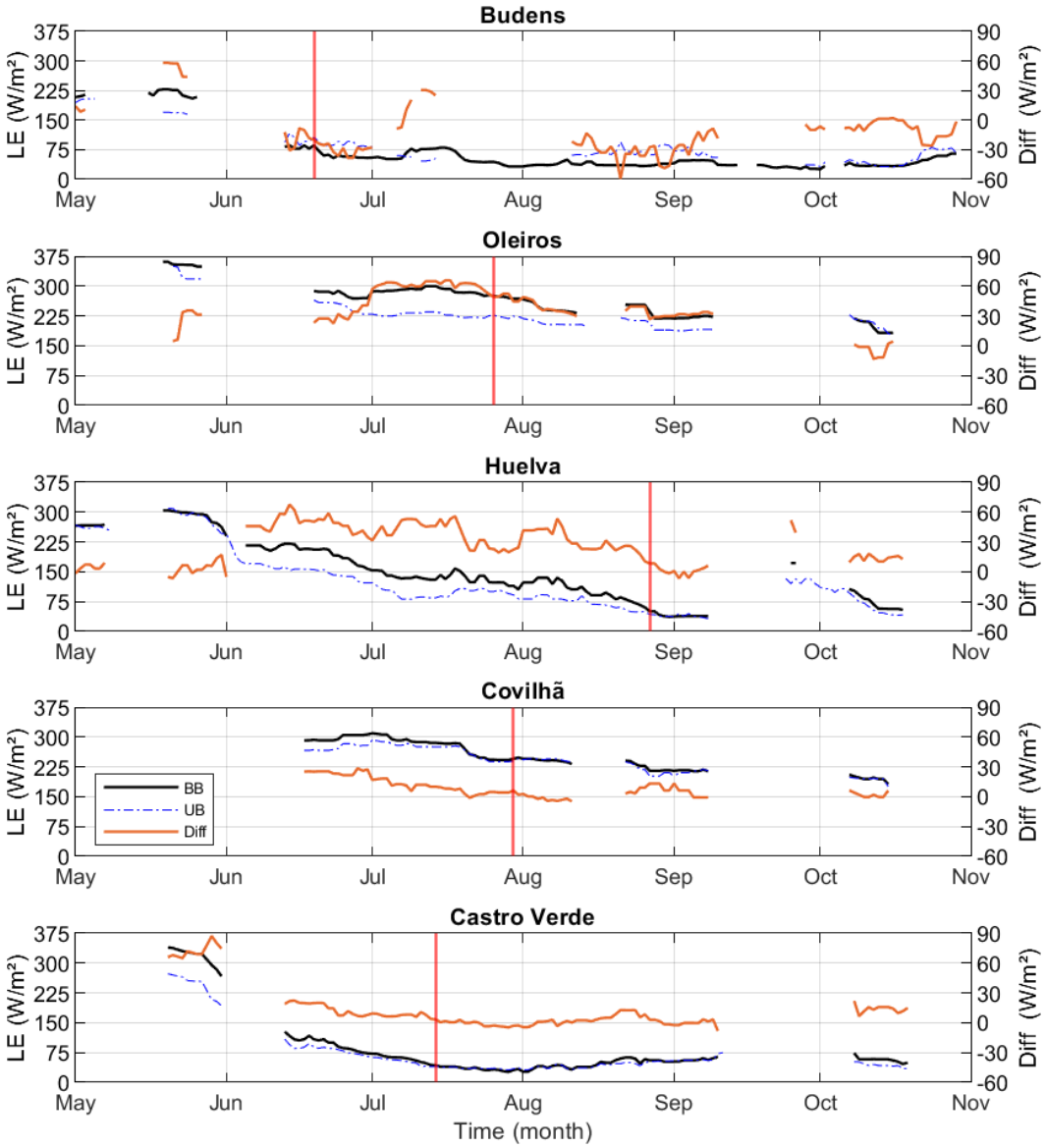

Figure 4.13 - As in Figure 4.1 but for Latent Heat Flux (LE).

4.2.5. Net Radiation

From Equation (2.1), it follows that the sum of latent (LE), sensible (H) and ground (G) heat fluxes equals the net radiation at the surface. Assuming that the contribution of the ground flux to the net radiation budget is reduced when compared to the other fluxes, we analyse the sum of the LE and H to study the impact of fire events on model simulated net radiation (Figure 4.14). For net radiation obtained from the model, there is no clear impact of fire events. There is a slight increase in net radiation in the case of Oleiros that occurs a few days after the fire, which is consistent with the observed increase in H (Figure 4.12).

Results presented in Figure 4.14 do not agree with the ones obtained with remote sensed data. To understand the role of the soil heat flux, G, in the net radiation, and of its possible impact in the fire events' signal, the soil heat flux was computed from the satellite data available. From Equation (2.4), it follows that β (i.e. the parameter used to compute G) increases with the decrease of LAI. We found that LAI generally decreases after the fire, which is to be expected given the reduction in vegetation (Figure 8.1 of the appendix). This decrease is well shown in Oleiros and Huelva, and is not as clear in Budens,

Covilhã and Castro Verde, which have, respectively, the highest and lowest burned area fractions. However, the highest increases in G are observed in Oleiros and Budens, while Huelva shows a weaker increase (Figure 8.2 of the appendix; no changes in G were observed in Covilhã and Castro Verde). Likely, the decrease in net radiation obtained from satellite data (Figure 4.9) compensates some of the increase due to the change in LAI.

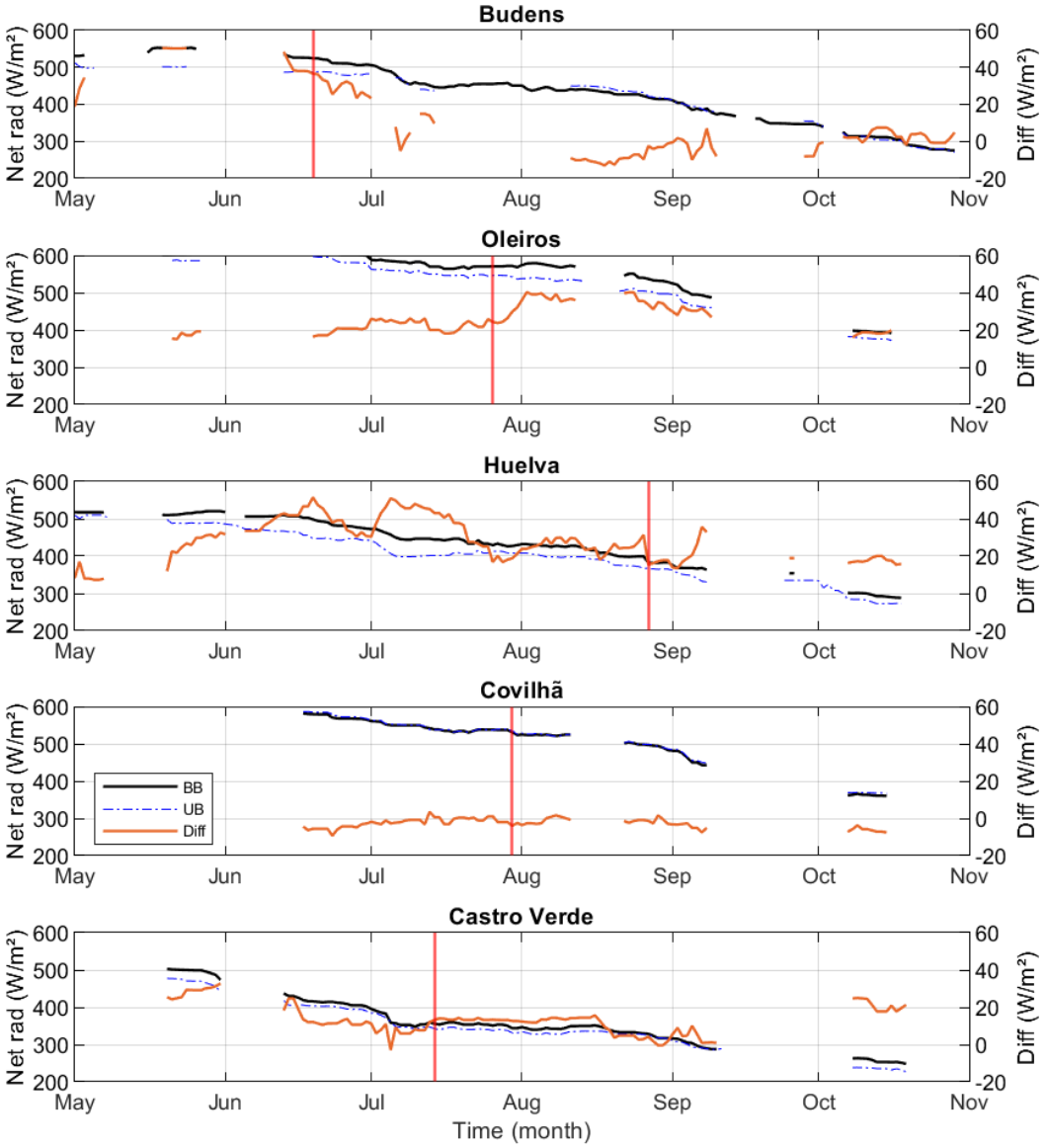

Figure 4.14 - As in Figure 4.1 but for Net radiation (computed with retrieved data from the model).

Figure 4.15 shows the time series of averaged net radiation for BB pixels as obtained from satellite data (SW+LW), and from model data as the sum (LE+H+G) or as the sum (LE+H), i.e. including or disregarding the ground flux G. It should be noted that G is estimated from satellite data and does not necessarily match the model estimated values, given that in the case of the model the net radiation is obtained by solving the energy balance. Even though G does not always match the model-estimated values, results obtained when summing G, LE and H, are closer to the net radiation values obtained from satellite data (Figure 4.9). The same is true in the case of the UB pixels (Figure 8.3, appendix).

For most events, there is no significant signal of the fire event on the modelled net radiation time-series. The only exception is Oleiros where there is an increase of net radiation that seems to be

linked to an increase in G. Such increase could be however an artifact from using G values that are not estimated by the model.

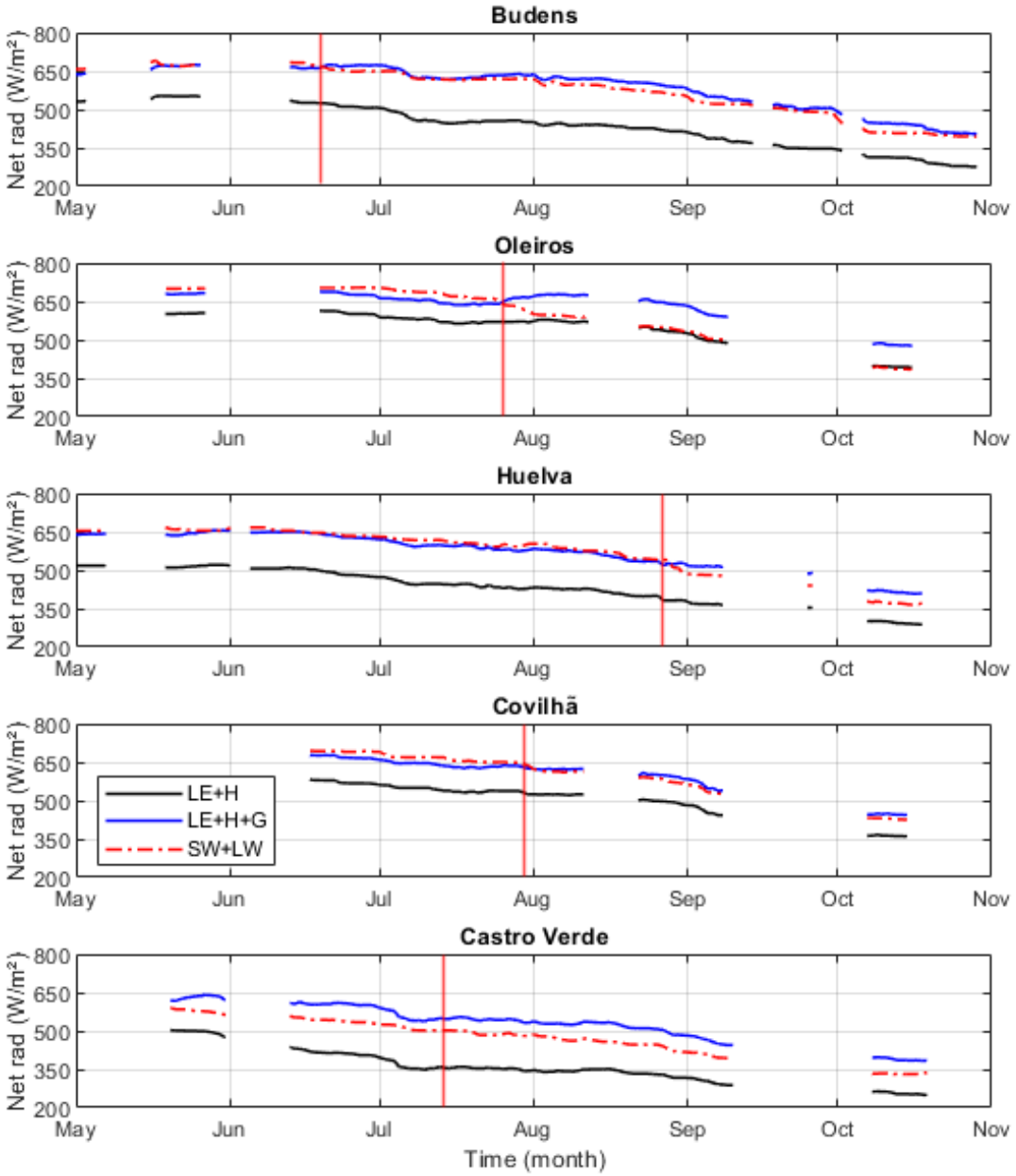

Figure 4.15 - Time series from May to October 2020 for all studied fires of Net radiation computed for burned (BB) pixels of studied events: 1) as the sum of LE and H (solid black lines); 2) as the sum of LE, H and G (solid blue lines); 3) as the sum of SW and LW balances (red dash-point lines). The vertical lines identify the starting dates of the wildfire events.

5 Discussion

Time series of DSSF (Figure 4.1) and DSLF (Figure 4.3) show that the two parameters are virtually not affected by fire events. Both parameters mostly depend on atmospheric conditions and therefore have reduced sensitivity to changes on surface properties, like soil or vegetation. However, in case there are large smoke plumes, both parameters will likely be affected as smoke may block part of the radiation reaching the surface (Petitcolin & Vermote, 2002).

Surface albedo is a parameter that depends on the properties of the surface. For instance, brighter surfaces have higher albedos, reflecting more radiation, while darker ones have lower values of albedo, reflecting less radiation (Beringer et al., 2003). Considering changes in soil properties, especially the darkening of the surface, it is expected that albedo will decrease after a fire event. On the other hand, since emissivity of vegetated surfaces is generally larger, it is expected that the emissivity will also decrease. The magnitude of changes in AL and EM will depend on land cover type (Chambers et al., 2005; Silva, 2020), as well as on the fraction of pixels that burned (Beringer et al., 2003). Cases where observed decreases in both AL (Figure 4.4) and EM (Figure 4.5) are larger are Oleiros and Huelva. Budens also has a high burned pixel fraction, however while AL changes are very pronounced, EM changes, while observable, are not as prominent. An increase in albedo is also observed after 1 to 2 months of the fire event due to the recovery of vegetation (short vegetation) as well as the scattering of the ash and char deposited on the ground (Bremer & Ham, 1999; Tsuyuzaki et al., 2009). It should be noted that while the burned area in Castro Verde is slightly higher than the burned area in Budens (Table 3.1), effects are more pronounced in Budens. This is a consequence of most of the burned area (Figure 3.1) being distributed through two pixels in Castro Verde, while in Budens it mostly concentrates in a single pixel.

LST is a surface parameter known to increase after a fire, considering the expected changes on the surface, e.g. in AL and EM. The decrease in these parameters contributes to a higher absorption of radiation by the surface and therefore to an increase in LST (Figure 4.6). It also depends on land cover type and the degree to which the analysed area was burned. An increase in LST is observed in all cases ranging from increases of 1.5 $°C$ in Castro Verde to $10°C$ in Oleiros and Huelva.

Shortwave (Figure 4.7) and longwave (Figure 4.8) balances were computed using satellite-derived data. The SW balance depends on DSSF and albedo. Changes in DSSF, as well as in DSLF, are negligible, however AL changes contribute to post fire changes in the SW balance. As decreases in albedo are observed, an increase in SW balance is expected. While such increase is noticeable, it is however negligible in most cases. The highest increase observed is in Oleiros, in agreement with the highest observed decreases in albedo. For the LW balance, changes are more noticeable. This balance depends on DSLF, EM and LST. While changes in DSLF are negligible, the observed decrease in EM and increase in LST will contribute to a decrease in LW balance. This decrease is especially conspicuous in Budens, Oleiros and Huelva.

The net radiation (Figure 4.9) was also analysed. Considering the highest observed increase of SW balance of about 25 Wm^{-2} (Oleiros) and observed decrease in LW balance of about 60 Wm^{-2} (Oleiros and Huelva) and that, in absolute value, the differences in LW balance are usually higher than in SW balance, it is expected a decrease of net radiation. That decrease is observed for all cases except Castro Verde. This is also the case where the mean burned fraction of the analysed pixels is smaller. One can therefore infer that the most important driver of the decrease is LST, due to its impact on the LW balance. LST is the variable where the largest changes are observed, and it also contributes as a power of four to the LW balance.

An alternate approach to study the net radiation is by adding up the surface heat fluxes using data from LSASAF's SEB model. The first variable studied is the skin temperature (Figure 4.10). This

variable can act as a diagnostic parameter as it should be comparable to the satellite-based LST (Figure 4.6). Given the results obtained, TSK, as LST, should increase considerably after the fires. Such large increase is only verified for Oleiros and Huelva (the largest fires), however even in these two cases, the modelled increase is, at most, half of the one observed in LST. Results indicate that the model is most likely not reproducing accurately the fire induced changes on the surface energy balance.

The evapotranspiration (Figure 4.11) and latent heat flux (Figure 4.13) can be analysed together, as evapotranspiration is a direct result of the latent heat flux (2.7). The scorching of the vegetation will reduce transpiration resulting in a decrease in evapotranspiration, as well as in a change in the partitioning of the energy (decrease of latent heat flux). A decrease in latent heat flux and an increase in sensible heat flux is also expected (Wendt et al., 2007). As referred in previous studies (Beringer et al., 2003; Chambers & Chapin, 2003; Wendt et al., 2007), a decrease in both ET and LE is anticipated and is observed in all cases, but it is not very pronounced in most of the areas studied.

The sensible heat flux (Figure 4.12), as mentioned in previous studies (Beringer et al., 2003; Chambers et al., 2005; Chambers & Chapin, 2003; Wendt et al., 2007) is expected to increase, as a result of the increase in surface temperature, which is observed in all areas except Budens. Both sensible and latent heat fluxes are considered in a first approach to the computation of the net radiation, neglecting however the ground heat flux. In this first approach, G is neglected since, unlike LE and H, it is not available as an output variable from SEB model. The net radiation (Figure 4.14) should be comparable to the values obtained from the satellite-based variables (Figure 4.9). In all cases, the values are always smaller than the satellite-based ones and only for Oleiros and Huelva do the modelled results show significant decreases in net radiation.

With the objective of better understanding the observed difference between the diagnosed and modelled net radiation, in this work, the ground heat flux, which had been previously neglected, is now taken into account. The ground heat flux (Figure 8.2 of the appendix) is computed from the diagnosed net radiation and LAI (Figure 8.1 of the appendix), which is also retrieved from LSASAF. The burning of the vegetation causes a drop in LAI, which, consequently, causes an increase in G. This increase is accentuated by the changes in properties of the soil like albedo, emissivity and surface temperature (Wendt et al., 2007). Both the decrease in LAI and the consequent increase in G are observed in the respective figures, presenting more noticeable changes for fire events with more vegetation prior to the fire, as well as higher burned fractions in the analysed pixels (Huelva, Oleiros and Budens).

When computing the net radiation (Figure 4.15), considering not only the sensible and latent heat fluxes, but also the ground heat flux, results obtained are closer to the ones obtained from the SW and LW radiation balances. This shows that the ground heat flux should not be neglected. For Castro Verde and Oleiros after the fire, when G is considered, the net radiation becomes larger than the one computed from remote-sensed data. It should be noted that the values of G used here are not necessarily the same as the ones estimated by the model. While, in this work, the net radiation was computed considering the remote-sensed LST, the model solves the TSK, LE, H and G relationship, and therefore computes the net radiation simultaneously. Although the LSA-SAF SEB model incorporates satellite-based products such as DSSF, DSLF, AL and LAI, it seems to be unable to reproduce the abrupt changes caused by fire events. Likely, this is related to the constrains imposed by the ECOCLIMAP database, which is used to define the landcover and fractions of high and low vegetation.

This study was carried out using data retrieved from satellite observations and data estimated by a SEB model. Satellite LST cannot be estimated under cloudy conditions and, therefore, the study presents the limitation of being restricted to clear-sky. The SEB model data present the advantage of being available under all-weather conditions. It should be also noted that the presence of clouds affected the satellite results obtained and the observed time-series were only possible due to a smoothing of the data available.

It is also important to stress that changes in the parameters, before and after the fire, are better represented in the larger wildfires. In some of the cases of smaller events, changes are barely noticeable. Extending the study to more burned areas and with larger burned scars would contribute to reduce uncertainties in the results obtained in this work.

6 Conclusion

Results from this study allow assessing the impacts of large wildfires on the surface energy balance. The assessment was made by studying several surface variables obtained from two sources: 1) satellite retrieved information; and 2) outputs from a surface energy model. All the wildfires analysed occurred during 2020 in the Iberian Peninsula, 4 of them in Portugal and 1 in Spain. Choice of these cases was based on the fraction of burned soil and the amount of data available.

Observed changes in the remote sensing variables are in accordance with previously performed studies (Amiro et al., 2020; Beringer et al., 2003; Chambers et al., 2005; Chambers & Chapin, 2003; Liu et al., 2018; Montes-Helu et al., 2009; Veraverbeke et al., 2012; Wendt et al., 2007). The main differences in surface parameters before and after the fire events were observed in albedo, emissivity, and land surface temperature. Both albedo and emissivity presented a decrease after the fire, which was more evident in the largest fire events. In turn, land surface temperature, as expected from results obtained in previous studies, increases after the fire. This increase is observed in all analysed cases and agrees with the disappearance of vegetation in burned areas. Moreover, a net radiation decrease was found over the burned areas. This decrease seems to be mostly associated to a decrease in the longwave radiation balance, which in turn is mostly due to an increase in LST after the fire.

Surface variables obtained from the surface energy balance model showed negligible changes after the wildfires in most cases, as opposed to the findings when analysing remote-sensed data. The skin temperature, that was expected to follow the behaviour of the remotely sensed LST, showed increased values after the fire. However, the increasein TSKis at most half of the one observed in LST. Results with data from the SEB model also show an increase in sensible heat flux and a decrease in latent heat flux after the fire event, even if not very accentuated. When estimated as the sum of sensible and latent heat fluxes, the net radiation did not show the expected sharp decrease after the fire; and in the cases where a decrease was observed, it was considerably small. When the ground heat flux is added, an improvement is observed in the computed net radiation that translates into a better compatibility with the net radiation obtained from satellite data. Overall, the SEB model does not seem to be able to adequately represent the impact of a wildfire on the surface energy balance. This is particularly evident when analysing the skin temperature that should have a more similar signature to the satellite land surface temperature.

This work clearly shows how satellite data can be used to study changes in surface parameters and net radiation in post fire scenarios. It also shows how remote-sensed information can be used to validate results from surface energy balance models (in this case the SEB model developed by the LSASAF) and then identify the shortcomings of the data produced by the models.

In order to minimize some of the flaws that were found in the data from the model, several approaches could be taken. For instance, it would be important to disseminate the ground heat flux computed from the model, allowing a better understanding of the results produced by the model. Additionally, since the model uses static values retrieved from the ECOCLIMAP database to compute the fraction of vegetation in each pixel, there is no decrease in this parameter after a wildfire event. This might explain the low values of skin temperatures that were found after the fire. This shortcoming might be mitigated by replacing the static input fraction of vegetation cover by e.g. daily values.

7 References

Albergel, C., Balsamo, G., De Rosnay, P., Muñoz-Sabater, J., & Boussetta, S. (2012). A bare ground evaporation revision in the ECMWF land-surface scheme: Evaluation of its impact using ground soil moisture and satellite microwave data. *Hydrology and Earth System Sciences*, *16*(10), 3607–3620. https://doi.org/10.5194/hess-16-3607-2012

Amiro, B. D. (2001). Paired-tower measurements of carbon and energy fluxes following disturbance in the boreal forest. *Global Change Biology*, *7*(3), 253–268. https://doi.org/10.1046/j.1365-2486.2001.00398.x

Amiro, B. D., Archibald, S., Lehmann, C. E. R., Belcher, C. M., Bond, W. J., Bradstock, R. A., Daniau, A. L., Dexter, K. G., Forrestel, E. J., Greve, M., He, T., Higgins, S. I., Hoffmann, W. A., Lamont, B. B., McGlinn, D. J., Moncrieff, G. R., Osborne, C. P., Pausas, J. G., Price, O., … Hutley, L. B. (2020). SAF for Land Surface Analysis (LSA SAF) - Algorithm Theoretical Basis Document - Meteosat Second Generation Evapotranspiration (MET) Product Daily MET (DMET) Product. *Remote Sensing*, *12*(1), 1–33. https://doi.org/10.1007/s10546-006-9148-3

Amraoui, M., Liberato, M. L. R., Calado, T. J., DaCamara, C. C., Coelho, L. P., Trigo, R. M., & Gouveia, C. M. (2013). Fire activity over Mediterranean Europe based on information from Meteosat-8. *Forest Ecology and Management*, *294*, 62–75. https://doi.org/10.1016/j.foreco.2012.08.032

Balsamo, G., Viterbo, P., Beijaars, A., van den Hurk, B., Hirschi, M., Betts, A. K., & Scipal, K. (2009). A revised hydrology for the ECMWF model: Verification from field site to terrestrial water storage and impact in the integrated forecast system. *Journal of Hydrometeorology*, *10*(3), 623–643. https://doi.org/10.1175/2008JHM1068.1

Beringer, J., Hutley, L. B., Tapper, N. J., Coutts, A., Kerley, A., & O'Grady, A. P. (2003). Fire impacts on surface heat, moisture and carbon fluxes from a tropical savanna in northern Australia. *International Journal of Wildland Fire*, *12*(3–4), 333–340. https://doi.org/10.1071/wf03023

Bremer, D. J., & Ham, J. M. (1999). Effect of spring burning on the surface energy balance in a tallgrass prairie. *Agricultural and Forest Meteorology*, *97*(1), 43–54. https://doi.org/10.1016/S0168-1923(99)00034-9

Carrer, D. et al. Land Surface Albedo and Down-Welling Short-Wave Radiation Retrievals using High Frequency Observations from MSG Geostationary Satellite. in Geoscience and Remote Sensing Symposium, 2008. IGARSS 2008. IEEE International 5, V–487 (IEEE, 2008).

Carrer, D., Id, S. M., Lellouch, G., Ceamanos, X., Pinault, F., Freitas, S. C., & Id, I. F. T. (2018). *Land Surface Albedo Derived on a Ten Daily Basis from Meteosat Second Generation Observations : The NRT and Climate Data Record Collections from the EUMETSAT LSA SAF*. https://doi.org/10.3390/rs10081262

Carrer, D., Roujean, J., & Meurey, C. (2010). *Comparing Operational MSG / SEVIRI Land Surface Albedo Products From Land SAF With Ground Measurements and MODIS*. *48*(4), 1714–1728. https://doi.org/10.1109/TGRS.2009.2034530

Chambers, S. D., Beringer, J., Randerson, J. T., & Chapin, I. S. (2005). Fire effects on net radiation and energy partitioning: Contrasting responses of tundra and boreal forest ecosystems. *Journal of Geophysical Research D: Atmospheres*, *110*(9), 1–9. https://doi.org/10.1029/2004JD005299

Chambers, S. D., & Chapin, F. S. (2003). Fire effects on surface-atmosphere energy exchange in Alaskan black spruce ecosystems: Implications for feedbacks to regional climate. *Journal of Geophysical Research: Atmospheres*, *108*(1), 1–17. https://doi.org/10.1029/2001jd000530

Ermida, S. L., Trigo, I. F., DaCamara, C. C., Göttsche, F. M., Olesen, F. S., & Hulley, G. (2014). Validation of remotely sensed surface temperature over an oak woodland landscape — The problem of viewing and illumination geometries. *Remote Sensing of Environment*, *148*, 16–27. https://doi.org/10.1016/J.RSE.2014.03.016

Freitas, S. C., Trigo, I. F., Bioucas-Dias, J. M., & Göttsche, F. M. (2010). Quantifying the uncertainty of land surface temperature retrievals from SEVIRI/Meteosat. *IEEE Transactions on Geoscience and Remote Sensing*, *48*(1), 523–534. https://doi.org/10.1109/TGRS.2009.2027697

García-haro, F. J., Coca, F. C., & Meliá, J. (2006). *A Directional Spectral Mixture Analysis Method : Application to Multiangular Airborne Measurements*. *44*(2), 365–377. https://doi.org/10.1109/TGRS.2005.861008

Ghilain, N. Algorithm Theoretical Basis Document Meteosat Second Generation based products Instantaneous Evapotranspiration (MET v2), Daily Evapotranspiration (DMET v2), Surface Latent Heat Flux (LE), Surface Sensible Heat Flux (H); SAF/LAND/RMI/ATBD_ETv2HLE/1.1; Land Surface Analysis Satellite Application Facility: Lisbon, Portugal, 2016; Available online: http://lsa-saf.eumetsat.int/ (accessed on 15 September 2020).

Ghilain, N., Arboleda, A., & Gellens-Meulenberghs, F. (2011). Evapotranspiration modelling at large scale using near-real time MSG SEVIRI derived data. *Hydrology and Earth System Sciences*, *15*(3), 771–786. https://doi.org/10.5194/hess-15-771-2011

Ghilain, N., Arboleda, A., Sepulcre-Cantò, G., Batelaan, O., Ardö, J., & Gellens-Meulenberghs, F. (2012). Improving evapotranspiration in a land surface model using biophysical variables derived from MSG/SEVIRI satellite. *Hydrology and Earth System Sciences*, *16*(8), 2567–2583. https://doi.org/10.5194/hess-16-2567-2012

Gorelick, N., Hancher, M., Dixon, M., Ilyushchenko, S., Thau, D., & Moore, R. (2017). Google Earth Engine: Planetary-scale geospatial analysis for everyone. *Remote Sensing of Environment*, *202*, 18–27. https://doi.org/10.1016/j.rse.2017.06.031

Huang, S., Dahal, D., Singh, R., Liu, H., Young, C., & Liu, S. (2013). Spatially explicit surface energy budget and partitioning with remote sensing and flux measurements in a boreal region of Interior Alaska. *Theoretical and Applied Climatology*, *113*(3–4), 549–560. https://doi.org/10.1007/s00704-012-0806-8

Instituto de Conservação da Natureza e das Florestas (2020). *Relatório provisório de incêndios florestais 2020, 01 de Janeiro a 15 de Outubro. Versão 8*

Kunkel, K. E. (2001). Surface Energy Budget and Fuel Moisture. In E. A. Johnson & K. Miyanishi (Eds.), *Forest Fires (pp. 303–350)*. https://doi.org/10.1016/b978-012386660-8/50011-8

Liu, Z., Ballantyne, A. P., & Cooper, L. A. (2018). Increases in Land Surface Temperature in Response to Fire in Siberian Boreal Forests and Their Attribution to Biophysical Processes. *Geophysical Research Letters*, *45*(13), 6485–6494. https://doi.org/10.1029/2018GL078283

Martins, J. P. A., Trigo, I. F., Ghilain, N., Jimenez, C., Göttsche, F. M., Ermida, S. L., Olesen, F. S., Gellens-Meulenberghs, F., & Arboleda, A. (2019). An all-weather land surface temperature product based on MSG/SEVIRI observations. *Remote Sensing*, *11*(24). https://doi.org/10.3390/rs11243044

Ministerio para la Transición Ecológica y el Reto Demográfico (2021). *Los incêndios florestales en España 1 de enero – 31 de diciembre 2020.* Avance Informativo

Miyanishi, K. (2001). Chapter 13 - Duff Consumption. In E. A. Johnson & K. Miyanishi (Eds.), *Forest Fires (pp. 437–475)*. Academic Press. https://doi.org/10.1016/B978-012386660-8/50015-5

Montes-Helu, M. C., Kolb, T., Dore, S., Sullivan, B., Hart, S. C., Koch, G., & Hungate, B. A. (2009). Persistent effects of fire-induced vegetation change on energy partitioning and evapotranspiration in ponderosa pine forests. *Agricultural and Forest Meteorology*, *149*(3–4), 491–500. https://doi.org/10.1016/j.agrformet.2008.09.011

Norman, J. M., & Becker, F. (1995). Terminology in thermal infrared remote sensing of natural surfaces. *Agricultural and Forest Meteorology*, *77(3–4)*, *153–166*. https://doi.org/10.1016/0168-1923(95)02259-Z

Pausas, J. G. (2004). Changes in fire and climate in the eastern Iberian Peninsula in the (Mediterranean basin). *Climatic Change*, *63*, 337–350. https://doi.org/10.1023/B:CLIM.0000018508.94901.9c

Pausas, J. G., & Vallejo, V. R. (1999). The role of fire in European Mediterranean ecosystems. *Remote Sensing of Large Wildfires*, *3–16*. https://doi.org/10.1007/978-3-642-60164-4_2

Petitcolin, F., & Vermote, E. (2002). Land surface reflectance, emissivity and temperature from MODIS middle and thermal infrared data. *Remote Sensing of Environment*, *83*(1–2), 112–134. https://doi.org/10.1016/S0034-4257(02)00094-9

Pinto, M. M., Libonati, R., Trigo, R. M., Trigo, I. F., DaCamara, C. C., Pinto, M. M., Libonati, R., Trigo, R. M., Trigo, I. F., & DaCamara, C. C. (2020). A deep learning approach for mapping and dating burned areas using temporal sequences of satellite images. *JPRS*, *160*, 260–274. https://doi.org/10.1016/J.ISPRSJPRS.2019.12.014

Quintano, C., Fernández-Manso, A., Calvo, L., Marcos, E., & Valbuena, L. (2015). Land surface temperature as potential indicator of burn severity in forest Mediterranean ecosystems. *International Journal of Applied Earth Observation and Geoinformation*, *36*, 1–12. https://doi.org/10.1016/j.jag.2014.10.015

Rother, D., & De Sales, F. (2020). Impact of Wildfire on the Surface Energy Balance in Six California Case Studies. *Boundary-Layer Meteorology*, *178*(1), 143–166. https://doi.org/10.1007/s10546-020-00562-5

Roujean, J. L., & Lacaze, R. (2002). Global mapping of vegetation parameters from POLDER multiangular measurements for studies of surface-atmosphere interactions: A pragmatic method and its validation. *Journal of Geophysical Research: Atmospheres*, *107*(12), ACL 6-1. https://doi.org/10.1029/2001jd000751

San-Miguel-Ayanz, J., Moreno, J. M., & Camia, A. (2013). Analysis of large fires in European Mediterranean landscapes: Lessons learned and perspectives. *Forest Ecology and Management*, *294*, 11–22. https://doi.org/10.1016/j.foreco.2012.10.050

Silva, A. M. (2020). Recuperação biofísica nas cicatrizes de incêndio (Masters thesis, Faculty of Sciences of University of Lisbon, Lisbon, Portugal). Retrieved from https://repositorio.ul.pt/handle/10451/45211

Trigo, I. F., Barroso, C., Viterbo, P., Freitas, S. C., & Monteiro, I. T. (2010). *Estimation of downward long - wave radiation at the surface combining remotely sensed data and NWP data*. *115*, 1–14. https://doi.org/10.1029/2010JD013888

Trigo, I. F., Dacamara, C. C., Viterbo, P., Roujean, J. L., Olesen, F., Barroso, C., Camacho-De-Coca, F., Carrer, D., Freitas, S. C., García-Haroj, J., Geiger, B., Gellens-Meulenberghs, F., Ghilain, N., Meliá, J., Pessanha, L., Siljamo, N., & Arboleda, A. (2011). The satellite application facility for land surface analysis. *International Journal of Remote Sensing*, *32*(10), 2725–2744. https://doi.org/10.1080/01431161003743199

Trigo, I. F., Ermida, S. L., Martins, P. A., Gouveia, C. M., Göttsche, F.-M., & Freitas, S. C. (2021). Validation and consistency assessment of land surface temperature from geostationary and polar orbit platforms: SEVIRI/MSG and AVHRR/Metop. *ISPRS Journal of Photogrammetry and Remote Sensing*, *175*, 282–297. https://doi.org/10.1016/j.isprsjprs.2021.03.013

Trigo, I. F., Monteiro, I. T., Olesen, F., & Kabsch, E. (2008). An assessment of remotely sensed land surface temperature. *Journal of Geophysical Research Atmospheres*, *113*(17), 1–12. https://doi.org/10.1029/2008JD010035

Trigo, I. F., Peres, L. F., DaCamara, C. C., & Freitas, S. C. (2008). Thermal land surface emissivity retrieved from SEVIRI/Meteosat. *IEEE Transactions on Geoscience and Remote Sensing*, *46*(2), 307–315. https://doi.org/10.1109/TGRS.2007.905197

Tsuyuzaki, S., Kushida, K., & Kodama, Y. (2009). Recovery of surface albedo and plant cover after wildfire in a Picea mariana forest in interior Alaska. *Climatic Change*, *93*(3–4), 517–525. https://doi.org/10.1007/s10584-008-9505-y

Van den Hurk, B. J. J. M., Viterbo, P., Beljaars, A. C. M., & Betts, A. K. (2000). *Offline validation of the ERA40 surface scheme*. *295*. https://doi.org/10.21957/9aoaspz8

Veraverbeke, S., Gitas, I., Katagis, T., Polychronaki, A., Somers, B., & Goossens, R. (2012). Assessing

post-fire vegetation recovery using red–near infrared vegetation indices: Accounting for background and vegetation variability. *ISPRS Journal of Photogrammetry and Remote Sensing*, *68*(1), 28–39. https://doi.org/10.1016/J.ISPRSJPRS.2011.12.007

Viterbo, P., & Beljaars, A. C. M. (1995). An improved land surface parameterization scheme in the ECMWF model and its validation. *Journal of Climate* (Vol. 8, Issue 11, pp. 2716–2748). https://doi.org/10.1175/1520-0442(1995)008<2716:AILSPS>2.0.CO;2

Wang, K., Wan, Z., Wang, P., Sparrow, M., Liu, J., Zhou, X., & Haginoya, S. (2005). Estimation of surface long wave radiation and broadband emissivity using moderate resolution imaging spectroradiometer (MODIS) land surface temperature/emissivity products. *Journal of Geophysical Research D: Atmospheres*, *110*(11), 1–12. https://doi.org/10.1029/2004JD005566

Wendt, C. K., Beringer, J., Tapper, N. J., & Hutley, L. B. (2007). Local boundary-layer development over burnt and unburnt tropical savanna: An observational study. *Boundary-Layer Meteorology*, *124*(2), 291–304. https://doi.org/10.1007/s10546-006-9148-3

8 Appendix

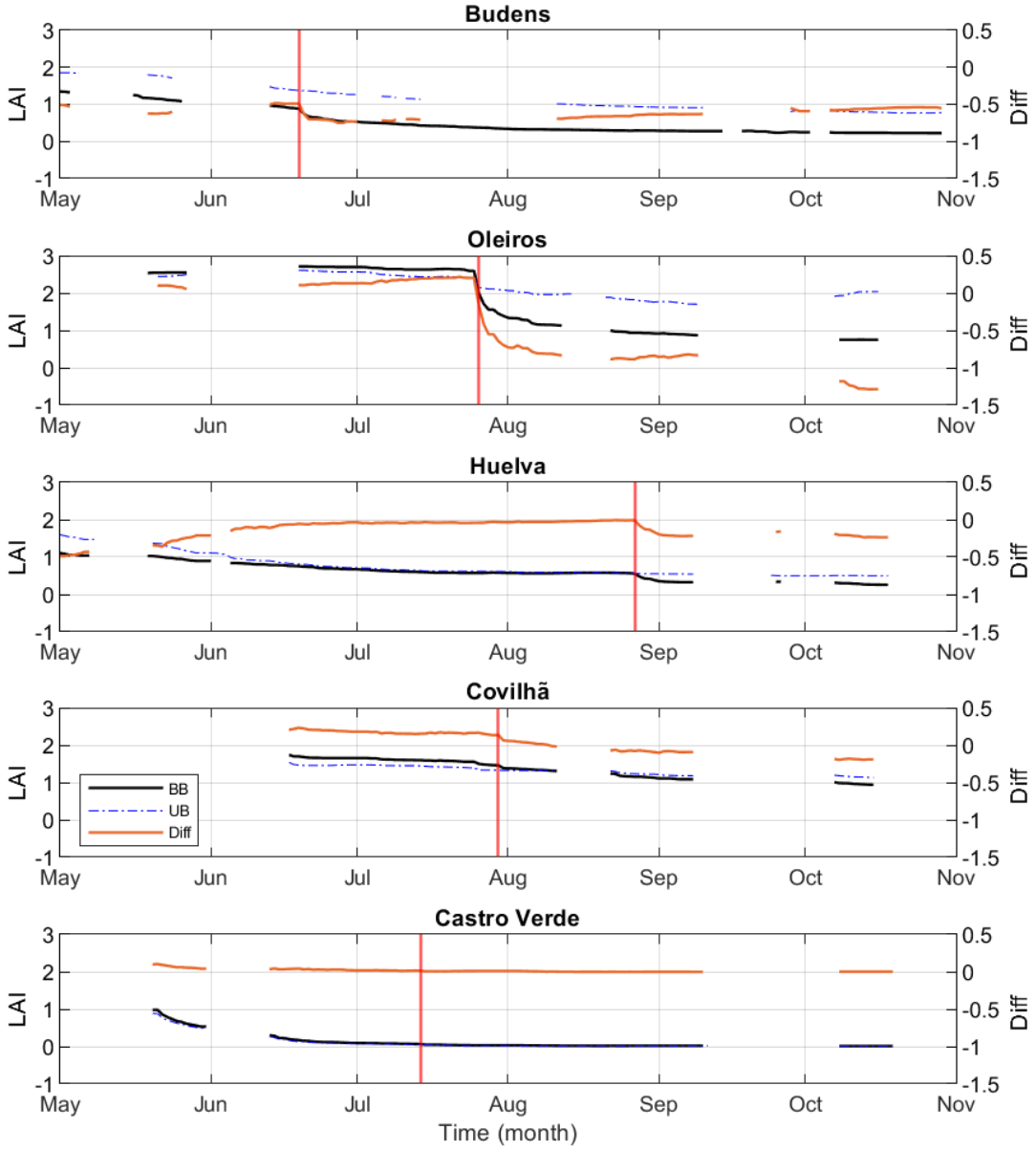

Figure 8.1 - As in Figure 4.1 but for Leaf Area Index (LAI).

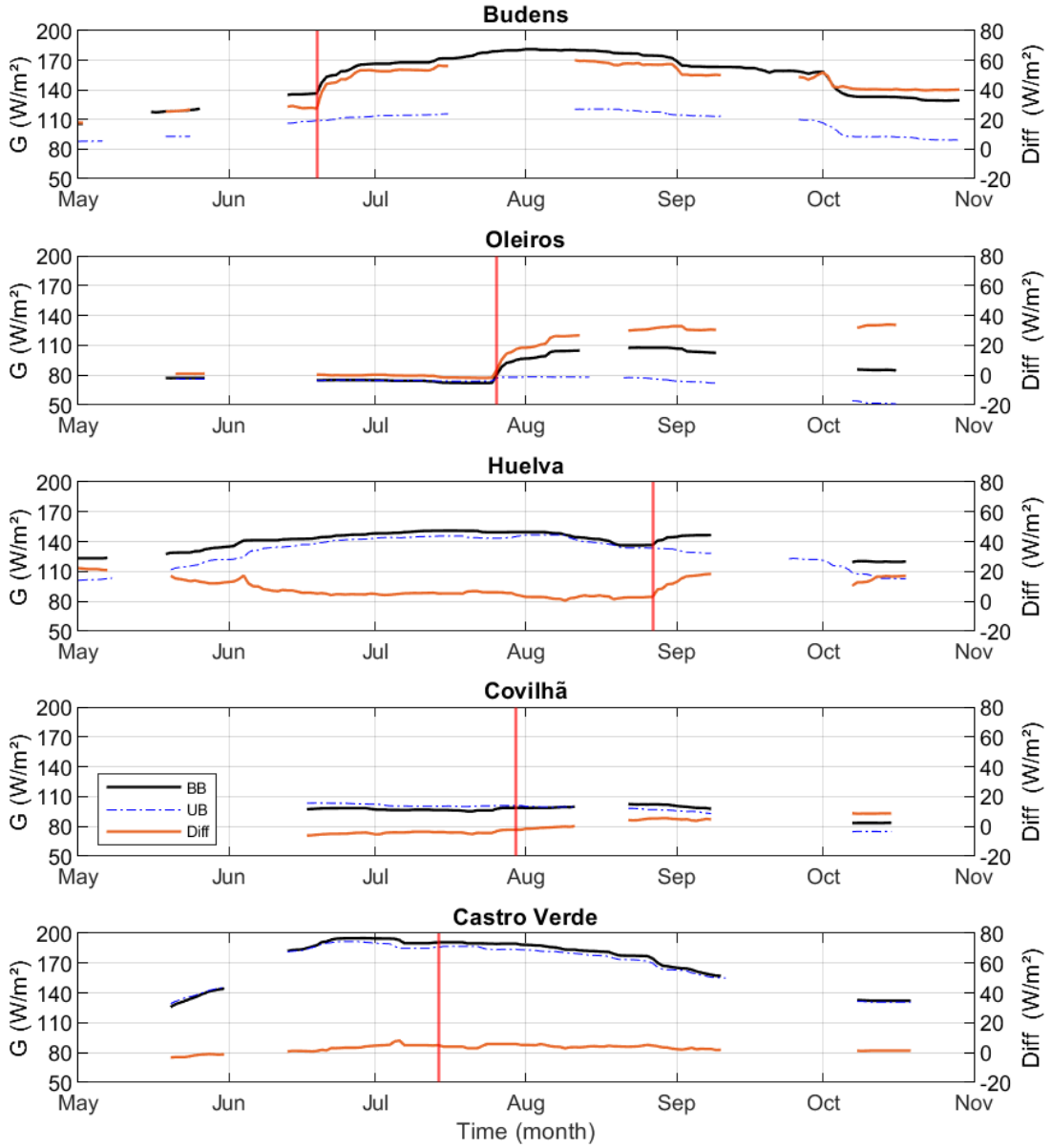

Figure 8.2 - As in Figure 4.1 but for Soil Heat Flux (G).

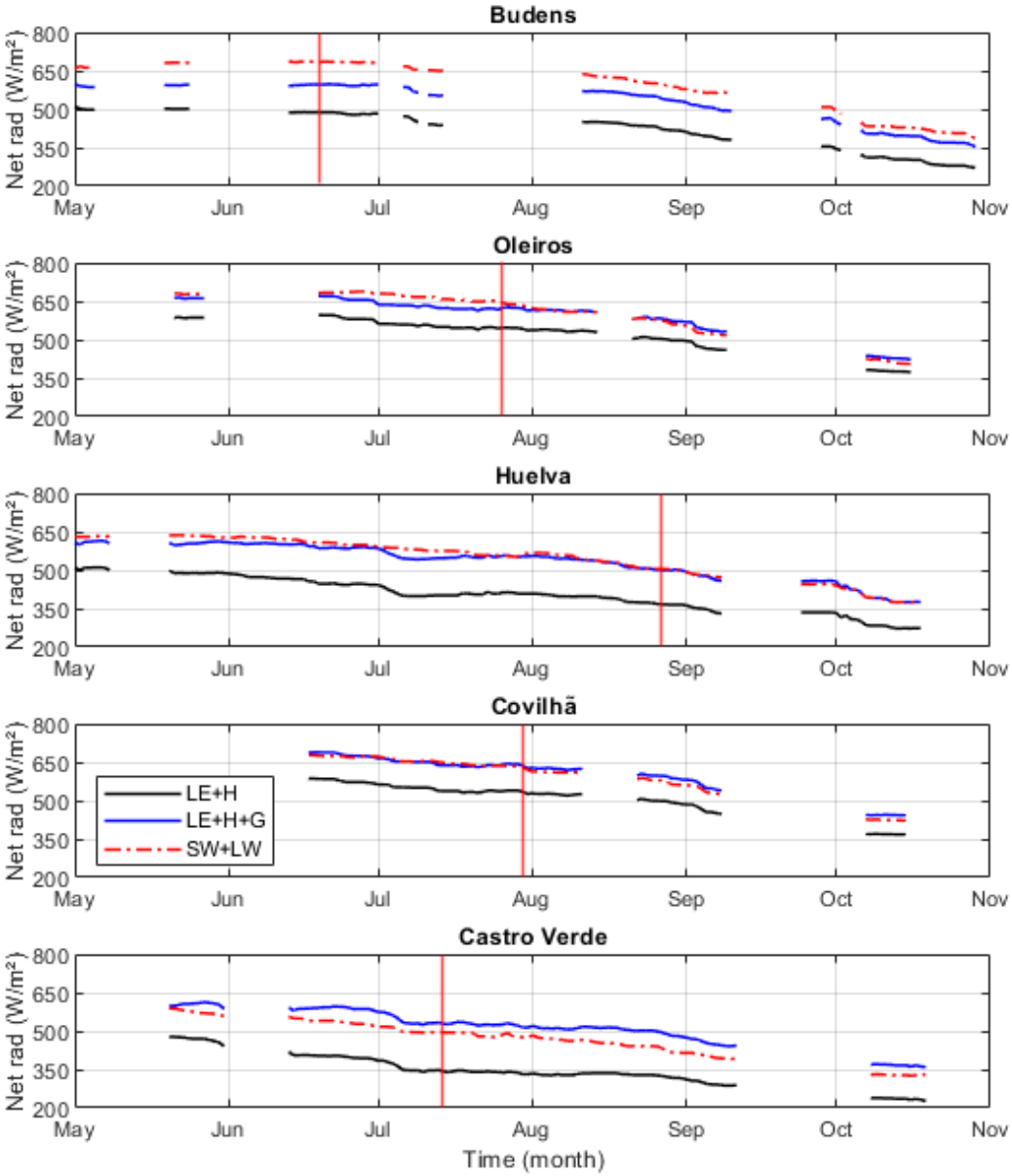

Figure 8.3 - As in Figure 4.15 but for Net radiation computed for unburned (UB) pixels.